AGU PUBLICATIONS

JGR

Journal of Geophysical Research: Space Physics

RESEARCH ARTICLE
10.1002/2014JA020890

Key Points:
- Overestimation of ionization rates of dayside compared with observations
- Short-lived ion densities are driven by local ionization
- Long-lived ion densities are influenced by chemical survival

Correspondence to:
L. B. M. Sagnières,
luc.sagnieres12@alumni.imperial.ac.uk

Citation:
Sagnières, L. B. M., M. Galand, J. Cui, P. P. Lavvas, E. Vigren, V. Vuitton, R. V. Yelle, A. Wellbrock, and A. J. Coates (2015), Influence of local ionization on ionospheri densities in Titan's upper atmosphere, *J. Geophys. Res. Space Physics*, *120*, 5899–5921, doi:10.1002/2014JA020890.

Received 27 NOV 2014
Accepted 19 JUN 2015
Accepted article online 30 JUN 2015
Published online 20 JUL 2015

Influence of local ionization on ionospheric densities in Titan's upper atmosphere

Luc B. M. Sagnières[1], Marina Galand[1], Jun Cui[2], Panayotis P. Lavvas[3], Erik Vigren[4], Véronique Vuitton[5], Roger V. Yelle[6], Anne Wellbrock[7], and Andrew J. Coates[7]

[1]Department of Physics, Imperial College London, London, UK, [2]Key Laboratory of Lunar and Deep Space Exploration, National Astronomical Observatories, Chinese Academy of Sciences, Beijing, China, [3]Groupe de Spectrométrie Moléculaire et Atmosphérique, Université de Reims, Reims, France, [4]Swedish Institute of Space Physics,Uppsala, Sweden, [5]Institut de Planétologie et d'Astrophysique de Grenoble, Grenoble, France, [6]Lunar and Planetary Laboratory, University of Arizona, Tucson, Arizona, USA, [7]Mullard Space Science Laboratory, University College London, Dorking, UK

Abstract Titan has the most chemically complex ionosphere of the solar system. The main sources of ions on the dayside are ionization by EUV solar radiation and on the nightside include ionization by precipitated electrons from Saturn's magnetosphere and transport of ions from the dayside, but many questions remain open. How well do models predict local ionization rates? How strongly do the ionization processes drive the ionospheric densities locally? To address these questions, we have carried out an analysis of ion densities from the Ion and Neutral Mass Spectrometer (INMS) from 16 close flybys of Titan's upper atmosphere. Using a simple chemical model applied to the INMS data set, we have calculated the ion production rates and local ionization frequencies associated with primary ions N_2^+ and CH_4^+. We find that on the dayside the solar energy deposition model overestimates the INMS-derived N_2^+ production rates by a factor of 2. On the nightside, however, the model driven by suprathermal electron intensities from the Cassini Plasma Spectrometer Electron Spectrometer sometimes agrees and other times underestimates the INMS-derived N_2^+ production rates by a factor of up to 2–3. We find that below 1200 km, all ion number densities correlate with the local ionization frequency, although the correlation is significantly stronger for short-lived ions than long-lived ions. Furthermore, we find that, for a given N_2 local ionization frequency, CH_5^+ has higher densities on the dayside than on the nightside. We explain that this is due to CH_4 being more efficiently ionized by solar photons than by magnetospheric electrons for a given amount of N_2 ionization.

1. Introduction

Although Titan's ionosphere was first measured from the Voyager 1 spacecraft in 1980 [*Bird et al.*, 1997], the sources of the ionosphere have been under debate for many years. The Cassini spacecraft, which reached Saturn in 2004, has offered a rich data set of plasma measurements of Titan's upper atmosphere. Electron number densities, observed by the Radio and Plasma Wave Spectrometer (RPWS) Langmuir probe (LP), were found to reach 2500–3500 cm^{-3} on the moon's dayside and around 400–700 cm^{-3} on its nightside at peak altitudes of 1050 to 1250 km [*Ågren et al.*, 2009]. Based on measurements from the Ion and Neutral Mass Spectrometer (INMS), major ions have been observed to be $HCNH^+$ and $C_2H_5^+$ [*Cravens et al.*, 2006], while more than 50 ions contributing to the formation of molecules and aerosols have also been identified [*Vuitton et al.*, 2007]. An intricate organic chemistry in the upper atmosphere has also been determined due to the presence of stable carbon-nitrile compounds [*Vuitton et al.*, 2006, 2014]. Evidence was found for tholin formation at altitudes of around 1000 km [*Waite et al.*, 2007; *Vuitton et al.*, 2008]. Heavy negative ions (up to 13,800 amu/q) from the Cassini Plasma Spectrometer (CAPS) Electron Spectrometer (ELS) and RPWS/LP [*Coates et al.*, 2007, 2009; *Ågren et al.*, 2012; *Wellbrock et al.*, 2013; *Shebanits et al.*, 2013] and heavy positive ions (up to 350 amu/q) from analysis of CAPS Ion Beam Spectrometer (IBS), INMS, and RPWS/LP data [*Wahlund et al.*, 2009; *Crary et al.*, 2009] were discovered to populate Titan's atmosphere near and below 1000 km. In this altitude range, the electron population is depleted to the benefit of negatively charged aerosols and Titan's ionosphere behaves as a dusty plasma [*Lavvas et al.*, 2013; *Vigren et al.*, 2014].

Titan's dayside ionosphere (defined as regions with a solar zenith angle (SZA) smaller than 105°, due to its extended atmosphere) comes primarily from XUV solar radiation (0.1 to 100 nm), as shown by the strong SZA dependence of the electron number densities [*Ågren et al.*, 2009], although electron precipitation from

Saturn's magnetosphere is occasionally dominating at the terminators, as shown from radio occultation observations [*Kliore et al.*, 2011], and is revealed on the dayside when solar radiation is weak enough at lower altitudes [*Cravens et al.*, 2009; *Galand et al.*, 2010]. On the nightside (SZA > 105°), the sources of ions include precipitating electrons from Saturn's magnetosphere [*Cravens et al.*, 2009; *Gronoff et al*., 2009] and transport of the ion population surviving from the dayside where primary, short-lived ions are created to the nightside where they have been transformed into long-lived ions [*Cui et al.*, 2009a, 2010]. Primary ions are produced through the ionization of atmospheric neutrals N_2 and CH_4: N_2^+, N^+, and CH_4^+. They are quickly converted to heavier species, through ion-neutral reactions, while terminal ions are lost through electron dissociative recombination [*Cravens et al.*, 2006; *Vuitton et al.*, 2006, 2007]. Negative ions, initially not expected to be seen at the altitudes of the Cassini flybys but in the lower stratosphere, were found to be produced through dissociative electron attachment to neutral molecules, and the major loss was found to be associative detachment with radicals [*Vuitton et al*., 2009b]. Furthermore, *Lavvas et al*. [2013] showed that the growth of aerosols found in Titan's upper atmosphere was due to collisions between negatively charged particles and positive ions.

Cassini observations have been compared to predictions from energy deposition and photochemistry models in terms of ionospheric production rates and ion densities. *Robertson et al.* [2009] and *Mandt et al.* [2012] found that the total ionospheric densities agree reasonably well with INMS and RPWS/LP observations. Like *Vuitton et al.* [2007, 2009a], they, however, found that the number densities of CH_5^+, $C_2H_5^+$, and $HCNH^+$ were overestimated by photochemical models by a factor of typically 2–4, up to 10 [*Mandt et al.*, 2012], compared to observations. *Westlake et al.* [2012] found a good agreement between the modeled and observed densities of short-lived ions, including CH_3^+, tracer of N_2^+, and CH_4^+, but found that the models overestimate $HCNH^+$. *Vigren et al.* [2013] calculated electron number densities for seven dayside flybys and found that, though the energy deposition model reproduced well the shape of the observed electron number densities, the calculated magnitudes were systematically larger by a factor of 2 compared to the Cassini RPWS/LP observations. *Richard et al.* [2015a] compared dayside modeled production rates of CH_4^+ and N_2^+ to ones derived empirically and found a good agreement. On the nightside, *Vigren et al.* [2015] found a good agreement between observations and their model for electron number densities and number densities of primary ions N^+, CH_2^+, CH_3^+, and CH_4^+. *Richard et al.* [2015b] looked at N_2^+ and CH_4^+ production rates on Titan's nightside and demonstrated that modeled and empirical ion production rates were in agreement with electron precipitation above 1100 km, although their conclusions are strongly dependent on their magnetic field assumptions.

In light of the discrepancies between models and observations of the ionosphere, we focus on local ion production rates, our ability to model them, and their role as a source for ionospheric densities. In section 2, we present the Cassini data set used in the study. Section 3 describes the three approaches: (1) a chemical, empirical model based on Cassini INMS data, similar to the one developed by *Richard et al.* [2015a], (2) a solar energy deposition model driven by EUV radiation, and (3) an electron impact ionization model driven by CAPS/ELS electron intensities. All models rely on the neutral number densities measured by INMS. In section 4, the ion production rates from the three models are compared. We also assess and discuss the effect of local ionization on short-lived and long-lived ions as a function of the $N_2 \rightarrow N_2^+$ local ionization frequency. In that section, we also discuss the finding that CH_5^+ exhibits larger number densities on the dayside than on the nightside for a given $N_2 \rightarrow N_2^+$ local ionization frequency. In section 5, we summarize and review our findings.

2. Cassini Data Set

In this study, measurements from two instruments onboard the Cassini spacecraft were used to obtain in situ data of Titan's upper atmosphere: INMS and CAPS/ELS. INMS is an instrument that gives information on mass composition and densities of nonreactive neutral species, in closed-source neutral (CSN) mode, and ion species, in open-source ion (OSI) mode, up to 100 amu [*Waite et al.*, 2004]. CAPS/ELS is a hemispherical top-hat electrostatic analyzer that measures the velocity distribution of electrons with an energy range of 0.6 to 28,250 eV [*Young et al.*, 2004].

Titan flybys were selected for the present study based on the following conditions: (1) both the OSI and CSN modes were functioning, (2) INMS pointing was within 2° of ram, (3) the closest approach (C/A) altitude was lower than 1200 km, since at higher altitudes, ion densities are modified by large ion drift velocities [*Ma et al.*, 2006; *Mandt et al.*, 2012]. This left a total of 16 flybys, ranging from 16 April 2005 to 26 September 2012. The configuration and main characteristics of the flybys used in this study are described in Table 1.

Table 1. Configuration of Dayside and Nightside Flybys as Defined in Section 1[a]

			SZA (°)			Latitude (°)			Longitude (°)					
Flybys (<105°)	Date	C/A (km)	In	C/A	Out	In	C/A	Out	In	C/A	Out	LST (h)	SLT (h)	Subsolar Latitude (°)
Dayside														
T18	23-Sep-06	960	99	90	81	80	71	51	85	357	341	14.4	2.3	−15.5
T32o	13-Jun-07	965	128	107	86	64	84	74	23	2	216	1.3	13.6	−11.8
T36	02-Oct-07	973	87	67	49	−54	−60	−54	73	109	146	16.1	11.5	−10.2
T39	20-Dec-07	970	78	61	47	−79	−70	−51	97	177	194	11.5	11.4	−9
T40	05-Jan-08	1014	55	38	21	−18	−12	−4	112	130	148	14.5	11.3	−8.8
T48	05-Dec-08	960	20	25	41	−23	−10	3	161	179	195	10.4	10.4	−3.7
T51	27-Mar-09	962	79	84	90	−50	−30	−10	225	235	241	6.4	10.1	−1.9
T59o	24-Jul-09	955	134	112	91	−43	−62	−75	163	179	230	21.6	21.8	−0.1
T65[b]	12-Jan-10	1072	106	95	84	−67	−82	−81	17	358	229	4.7	16.9	2.5
T71	07-Jul-10	1003	98	82	66	−48	−56	−55	332	304	269	7.4	16.1	5.1
T83	22-May-12	954	93	71	50	66	73	60	66	128	172	16.9	13.7	14.3
T86	26-Sep-12	956	68	47	25	84	63	41	197	201	201	11.8	13.5	15.9
Nightside														
T5	16-Apr-05	1027	114	127	138	72	74	61	338	271	238	23.3	5.3	−21.7
T26	10-Mar-07	981	164	149	131	14	32	48	8	358	343	1.8	13.8	−13.1
T32i	13-Jun-07	965	128	107	86	64	84	74	23	2	216	1.3	13.6	−11.8
T50	07-Feb-09	966	124	136	141	−52	−34	−14	320	306	297	1.7	10.2	−2.7
T57	22-Jun-09	955	149	128	107	−23	−42	−59	166	178	200	21.8	21.9	−0.6
T59i	24-Jul-09	955	134	112	91	−43	−62	−75	163	179	230	21.6	21.8	−0.1
T65[b]	12-Jan-10	1072	106	95	84	−67	−82	−81	17	358	229	4.7	16.9	2.5

[a] "In" and "out" correspond to an altitude of 1200km along the inbound and outbound legs, respectively. C/A, SZA, LST, and SLT refer to closest approach altitude, solar zenith angle, local solar time, and Saturn local time, respectively. "i" and "o" after the flyby number define the inbound and outbound legs of the flybys, respectively.

[b] T65 inbound down to 1200 km is in the dayside while the inbound leg below 1200 km and the outbound leg are in the nightside.

The neutral number densities used were analyzed by and obtained from *Cui et al.* [2012] using a calibration factor of 2.9 [*Koskinen et al.*, 2011; *Westlake et al.*, 2012], while the ion densities were obtained using the method described by *Mandt et al.* [2012]. When calculating the ion number densities, a minimum transmission of 0.5 was adopted, as suggested by *Mandt et al.* [2012]. Points with a lower transmission usually witnessed abnormally larger densities. It has been suggested that new INMS calibration values should be adopted for both ion and neutral number densities [*Teolis et al.*, 2015]. We have adopted the new ion calibration of $1.55 \pm 21\%$. We have however kept the calibration factor of 2.9 for neutrals as it is within the uncertainties of the neutral number density values. Furthermore, this factor yields electron density profiles whose peak altitudes agree with observations from Cassini/RPWS/LP [*Vigren et al.*, 2013]. The effect of adopting the new neutral calibration of $2.2 \pm 23\%$ derived by *Teolis et al.* [2015] is discussed in section 4.

The suprathermal electron intensities from CAPS/ELS were obtained from the analysis described by *Lewis et al.* [2010]. The electron spectra are either from anode 2 or 3 of the instrument, as the spectra from the other anodes have a possibility of being polluted by negative ions. The signature of these ions appears in the spectra when the ram direction of the spacecraft is in the field of view of the anode. The sequence of negative ions appears over a large range of energy. The energy associated with a given ion species is a function of the mass of the ions and the spacecraft velocity, which is significantly larger than the ion velocities [*Coates et al.*, 2007; *Wellbrock et al.*, 2013]. The CAPS/ELS intensities were used for the calculation of electron and ion production rates for four nightside flybys during which CAPS/ELS data were available: T5, T50, T57, and T59 (see sections 3.3 and 4.1.2).

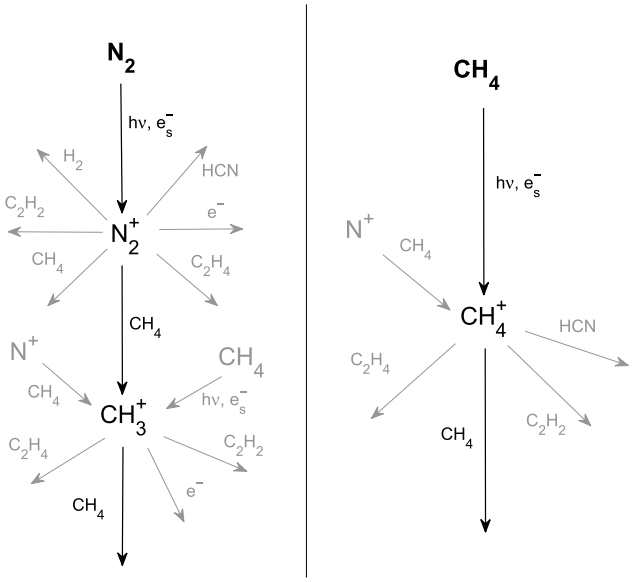

Figure 1. Chemical reactions considered for calculation of N_2^+ and CH_4^+ production rates. "hν, e_s^-" corresponds to ionization by solar photons and by impact with suprathermal electrons.

3. Modeling Tools and Key Parameters

To calculate the ion production rates and to assess the importance of local ionization at Titan, we have used three approaches: (1) a chemical model based on INMS neutral and ion number densities (see section 3.1), (2) a solar energy deposition model used on the dayside (see section 3.2), and (3) an electron impact ionization model based on CAPS/ELS used on the nightside (see section 3.3). In section 3.4, we discuss the derivation of local ionization frequency using the three models. Section 3.5 describes the ionospheric model that estimates the relationship between ion number density and local ionization frequency. Finally, section 3.6 characterizes the parameter used to define the amount of possible ionization.

3.1. Chemical Model From Production Rate Estimates

3.1.1. Computation of N_2^+ and CH_4^+ Production Rates

The chemical model assumes photochemical equilibrium, which is a reasonable assumption at the altitudes we are considering (< 1200 km), where transport timescales are longer than ion chemical lifetimes [*Robertson et al.*, 2009; *Cravens et al.*, 2010]. It uses both ion and neutral number densities observed by INMS to calculate the production rates of N_2^+ and CH_4^+ coming from the ionization of the parent neutral N_2 and CH_4, respectively. As Titan holds a very complex ionosphere, many chemical reactions take place. The reactions considered in the chemical model are described in Figure 1 for both the N_2^+ and CH_4^+ reaction pathways. However, for the calculation of the production rates, only the central reactions shown in black on the figure are considered. This simplifies the computation of the production rates to the main chemical pathways. In addition, it avoids using the number densities of the minor neutrals which are not exactly known. These calculations are similar to what has been done by *Richard et al.* [2015a].

No N_2^+ number densities are available from INMS since this ion shares the same mass as the major ion $HCNH^+$, which is more abundant by a few orders of magnitude. As a result, the number densities of CH_3^+ are commonly used as a proxy for the calculation of the N_2^+ production rates [*Westlake et al.*, 2012; *Richard et al.*,2015a]. From Figure 1, if we consider that all N_2^+ is lost through the production of CH_3^+, that all the CH_3^+ production comes from N_2^+, and that all CH_3^+ is lost from a reaction with CH_4, as shown by the black central reactions, then photochemical equilibrium applied to N_2^+ and CH_3^+ implies

$$P_{N_2^+} = L_{N_2^+} = P_{CH_3^+} = L_{CH_3^+} = k_1[CH_3^+][CH_4] \quad (1)$$

where k_1 is the reaction rate coefficient of the loss of CH_3^+ by reacting with CH_4.

Similarly, considering the black central reactions from Figure 1 for CH_4^+, if we assume that all CH_4^+ is produced from the ionization of CH_4 and that all CH_4^+ is lost from reaction with CH_4, then photochemical equilibrium applied to CH_4 yields

$$P_{CH_4^+} = L_{CH_4^+} = k_2[CH_4^+][CH_4] \quad (2)$$

where k_2 is the reaction rate coefficient of the loss of CH_4^+ by reacting with CH_4.

The reaction rate coefficients used are $k_1 = 1.10 \times 10^{-9}$ cm^3 s^{-1} and $k_2 = 1.14 \times 10^{-9}$ cm^3 s^{-1}, with an error of 20% and 15%, respectively [*McEwan and Anicich*, 2007]. The errors on the INMS ion number densities

Table 2. Summary of Type of Reactions Neglected for the Calculation of Production Rates of N_2^+ and CH_4^+ and the Corresponding Scale Factor for Correction

Neglected Reactions	Scale Factor (%)
N_2^+ sinks	67
CH_3^+ sources	85–89
CH_3^+ sinks	95
CH_4^+ sources	83
CH_4^+ sinks	93
Total for N_2^+	132–140
Total for CH_4^+	90

include counting statistics, a 10% systematic uncertainty in transmission, and a 15% systematic uncertainty in sensitivity [*Mandt et al.*, 2012]. Additionally, there is an error on the ion number density calibration value of 21% [*Teolis et al.*, 2015]. As mentioned by *Mandt et al.* [2012], uncertainties in spacecraft potential and ion velocities are not taken into account as they are difficult to determine but do propagate to uncertainties in calibrated number densities. The spacecraft potential is taken from the CAPS Ion Beam Spectrometer (IBS) instrument when available or from the Radio and Plasma Wave Science (RPWS) instrument otherwise, as IBS is closer to INMS than RPWS, thus giving a more accurate value of the potential. The ion velocities are taken from IBS when available, or otherwise a stationary background is assumed. The errors on the neutral number densities include counting statistics that range from 0.1% to 5% [*Cui et al.*, 2012] and a systematic uncertainty on the calibration factor of 2.9, typically around 25% [*Teolis et al.*, 2015]. The total error on ion production rates coming from the propagation of these uncertainties, other than the systematic uncertainty from the calibration factor, varies around 35% to 45% for both N_2^+ and CH_4^+, although they are generally higher for CH_4^+ due to its lower signal-to-noise ratio.

It is important to note that equations (1) and (2) do not consider the other chemical reactions in Titan's atmosphere shown in grey in Figure 1. It is possible to correct for the neglect of these reactions by multiplying the obtained production rates from equations (1) and (2) by a constant scale factor. Doing so adds an extra uncertainty that needs to be considered. This will be done in the following two sections for N_2^+ and CH_4^+. Table 2 outlines the factors that are derived from the neglect of each type of reaction.

3.1.2. Neglecting N_2^+ Reactions

If we start by considering the N_2^+ pathway, there are three different types of reactions we are neglecting. First, there are other ways in which N_2^+ is lost. The reaction rate coefficients for the loss of N_2^+ with H_2, CH_4, C_2H_2, and C_2H_4 are taken from *Dutuit et al.* [2013] and with HCN from *McEwan and Anicich* [2007], and the electron recombination coefficient is taken from *Peterson et al.* [1998] adjusted to the electron temperature from T40 at 1050 km of 585 K [*Vigren et al.*, 2013]. We consider the volume mixing ratios of *Cui et al.* [2009b] for H_2 and CH_4 at 1025 km, those of *Magee et al.* [2009] for C_2H_2, C_2H_4, and HCN at 1050 km, and an approximate electron number density of 2500 cm^{-3} at the same altitude from *Ågren et al.* [2009]. Under those conditions, 78% of the total N_2^+ loss comes from a reaction with CH_4. However, according to *Dutuit et al.* [2013], only 86% of the N_2^+ loss with CH_4 produces CH_3^+. This means that 67% of the N_2^+ loss results in the production of CH_3^+.

Second, there are also different CH_3^+ production pathways we are neglecting. By considering the reaction rate coefficients and yield of *Dutuit et al.* [2013] for the production of CH_3^+ from N_2^+ and N^+, the N_2^+ and N^+ number densities from T40 INMS/OSI data (the N_2^+ number density is approximated by scaling the CH_3^+ number density to the ratio of the loss reaction rate coefficients of N_2^+ and CH_3^+ with CH_4), and the CH_4 ionization from our solar energy deposition model using the T40 outbound conditions at 1050 km, we find that 85% of the CH_3^+ production comes from N_2^+. We also calculated this without ionization of CH_4 and found that in this case, 89% of the CH_3^+ production comes from N_2^+. This was done to include the case when ionization is much less important than the other reactions, which is true on Titan's nightside where there is no photoionization.

Third, there are losses of CH_3^+ that we are neglecting. When considering the reaction rate coefficients of *McEwan and Anicich* [2007] for the loss of CH_3^+ with CH_4, C_2H_2, and C_2H_4, the electron recombination coefficient of *Thomas et al.* [2012], and the same volume mixing ratios, electron number density, and electron temperature as mentioned above, we find that 95% of the total loss of CH_3^+ is due to a reaction with CH_4.

Combining the neglect of all of these reactions, the production rate of N_2^+ is found to be between 132% and 140% of the loss of CH_3^+ with CH_4. These values are approximate and also change with altitude since the volume mixing ratios and production rates from ionization changes with altitude. The explicit altitude dependence of the scale factor is hard to estimate as the volume mixing ratios of the neutrals are not exactly known

and differ for every flyby. In order to take these uncertainties into account, we introduce into equation (1) a constant multiplicative factor c_1 of 1.35. However, it should be kept in mind that this factor is variable and slightly altitude dependent and adds an uncertainty on the production rate values.

3.1.3. Neglecting CH_4^+ Reactions

In the case of CH_4^+, there are two sets of reactions we neglect. First, there are the other production pathways of CH_4^+ which are not from photoionization or electron impact ionization of CH_4. CH_4^+ can also be produced from a reaction of N^+ with CH_4. If we consider the reaction rate coefficient of *Dutuit et al.* [2013] from this loss process and the same number density of N^+ as mentioned in the case above, we find that 83% of the total production of CH_4^+ is from ionization of CH_4.

Second, if we look at the other losses of CH_4^+, by considering the reaction rate coefficients of *McEwan and Anicich* [2007] for the loss of CH_4^+ with HCN, CH_4, C_2H_2, and C_2H_4 and the same volume mixing ratios as described above, we find that 93% of the total loss of CH_4^+ is from a reaction with CH_4.

This means that the total production of CH_4^+ from photoionization and electron impact ionization is equal to approximately 90% of the loss of CH_4^+ with CH_4. We introduce a constant value of 0.9 for the multiplicative factor c_2 in equation (2) for calculating CH_4^+ production rates. A similar calculation was done at 1150 km, but this factor did not show any significant altitude dependence (the change in c_2 was below 1%). This factor is however approximate and adds another uncertainty to the production rate estimate.

3.2. Solar Energy Deposition Model

The solar energy deposition model calculates ion production rates for N_2^+ and CH_4^+ from photoionization by solving the Beer-Lambert law, as well as secondary ionization from electron impact assuming the local approximation when solving the Boltzmann equation for suprathermal electrons [*Lavvas et al.*, 2011]. The local approximation is justified as secondary ionization becomes dominant only in the deep ionosphere where the mean free path of photoelectrons and their secondaries is negligible. This model is used on dayside flybys for comparison to the chemical model.

As input, this model uses the daily averaged Thermosphere, Ionosphere, and Mesosphere Energetics and Dynamics (TIMED)/Solar EUV Experiment (SEE) solar flux measured at Earth and extrapolated in distance and phase to Saturn for the day of the flyby, below 80 nm with a 1 nm resolution [*Woods et al.*, 2005]. Above 80 nm, it uses a high-resolution (0.004 nm) solar flux from the SOHO/Solar Ultraviolet Measurements of Emitted Radiation instrument that is scaled to the ratio of the TIMED/SEE flux for each wavelength bin [*Curdt et al.*, 2013]. The photoabsorption cross sections used come from *Samson et al.* [1989] for CH_4 with the CH_4^+ ionization threshold of 12.61 eV or 98.3 nm. For N_2, the photoabsorption cross sections are from *Stolte et al.* [1998] below 12.4 nm, from *Fennelly and Torr* [1992] between 12.4 nm and 66 nm, from *Shaw et al.* [1992] from 66 nm to the ionization threshold of 15.58 eV or 79.6 nm, and from the coupled-channel Schrödinger equation (CSE) quantum mechanical model described by *Lavvas et al.* [2011] above 80 nm. Using high-resolution N_2 photoabsorption cross sections is necessary due to the highly structured shape of the cross sections resulting from the vibrational excitation of N_2, which has a strong effect on the CH_4^+ production rates at the altitude range we are considering [*Lavvas et al.*, 2011].

3.3. ELS Electron Impact Ionization Model

The third model, applied to the nightside, calculates the production rates of N_2^+ and CH_4^+ from CAPS/ELS intensities of suprathermal electrons. The production rate of an ion *i* from electron impact ionization of a neutral *n* is calculated as follows:

$$P_{n,i}^{e^-} = 2\pi n_n(z) \int_{E_{min}}^{E_{max}} dE \left[\int_{-1}^{1} d\mu \, I_e(z, E, \mu) \sigma_{n,i}^{e^-}(E) \right] \quad (3)$$

where n_n is the neutral number density of neutral species *n* (N_2 or CH_4). I_e is the suprathermal electron intensity, which is a function of altitude *z*, electron energy *E*, and electron pitch angle θ ($\mu = \cos\theta$). $\sigma_{n,i}^{e^-}$ is the electron impact ionization cross section associated with the ionization of the neutral *n* and yielding the production of the ion species *i*. E_{min} is the ionization threshold energy of the neutral *n* and E_{max} is the maximum energy channel for CAPS/ELS (≈28 keV). As we found that the production rates obtained from the electron intensities acquired for the two anodes used were below 10%, we assumed isotropy. In that case, the integral over μ is reduced to a factor of 2. The neutral number densities are from *Cui et al.* [2012], and the electron impact ionization cross sections are from *Shemansky and Liu* [2005] for N_2^+ and from *Liu and Shemansky* [2006]

for CH_4^+. The uncertainties in this model come from the accuracy of the cross sections (8%), from the uncertainties in the INMS neutral number densities (see section 3.1.1), and from the CAPS/ELS electron intensities. The latter is a combination of counting statistics and a random uncertainty due to the error on the geometric factor, which can range from 5% to 20% at higher energies. Furthermore, in the calculation of the production rates, the intensities were not corrected for spacecraft potential. This was however shown to only have a minor effect on the production rates, where including the spacecraft potential increases the production rates by less than 5% [*Vigren et al.*, 2015].

3.4. Local Ionization Frequency

The local ionization frequencies are used to assess the influence of local ionization on ion number densities. They represent the amount of possible ionization of a given neutral at a given altitude and SZA. It is the product of the amount of the ionization source at that point, either photons and/or suprathermal electrons, and the probability of ionization of a given neutral yielding the production of a given ion species. Theoretically, the local ionization frequency associated with the neutral *n* to be ionized and the produced ion *i* is calculated from both the solar energy deposition model (section 3.2) or ELS model (section 3.3), for N_2 or CH_4, as follows:

$$\nu_{n,i} = \int_{E_{min}}^{E_{max}} dE\, I(z,E)\sigma_{n,i}(E) \tag{4}$$

where I is the attenuated solar intensity or electron intensity and $\sigma_{n,i}$ is the photoionization cross section or electron impact ionization cross section, depending on the source of the ionization. The ionization frequencies also correspond to the production rates divided by the number density of the neutral species that are ionized. When applied to the chemical approach (see section 3.1), this yields the following expressions for the local ionization frequencies associated with $N_2 \rightarrow N_2^+$ and $CH_4 \rightarrow CH_4^+$:

$$\nu_{N_2,N_2^+} = c_1 \frac{k_1[CH_3^+][CH_4]}{[N_2]} \tag{5}$$

$$\nu_{CH_4,CH_4^+} = c_2 k_2 [CH_4^+] \tag{6}$$

3.5. Ionospheric Model From Ion Density Estimates

The relationship between ion density and local ionization frequency varies as a function of the sources and sinks of individual ions. In order to get a better understanding of how ion density depends on local ionization, we have developed an ionospheric model, neglecting transport, which is justified in the lower ionosphere (see section 3.1.1). Both the chemical model described in section 3.1 and the ionospheric model introduced in this section solve the continuity equation applied to ions. However, their purpose is very different. On the one hand, the chemical model is used to derive ion production rates and local ionization frequencies from INMS neutral and ion densities. On the other hand, the ionospheric model calculates the ion densities and relates them to the local ionization frequency. Three distinct approaches have been applied and are described in detail in Appendix A: (1) a theoretical approach to short-lived ions with no time dependence, (2) a theoretical approach to long-lived ions with no time dependence, (3) a time-dependent analytical model applied to short-lived and long-lived ions. In this simplified ionospheric model, we have assumed only the following reactions:

$$A + h\nu\ (\text{or } e^-) \rightarrow A^+ + e^-\ (+ e^-) \tag{7}$$

$$A^+ + B \rightarrow C^+ + D \tag{8}$$

$$C^+ + E \rightarrow F^+ + G \tag{9}$$

$$C^+ + e^- \rightarrow H_1 + H_2 \tag{10}$$

$$F^+ + e^- \rightarrow I_1 + I_2 \tag{11}$$

where A, B, D, E, G, H_1, H_2, I_1, and I_2 are neutrals, A^+ and C^+ are primary and intermediate short-lived ions, respectively, and F^+ is a long-lived ion. Under photochemical equilibrium, the ion density is related to

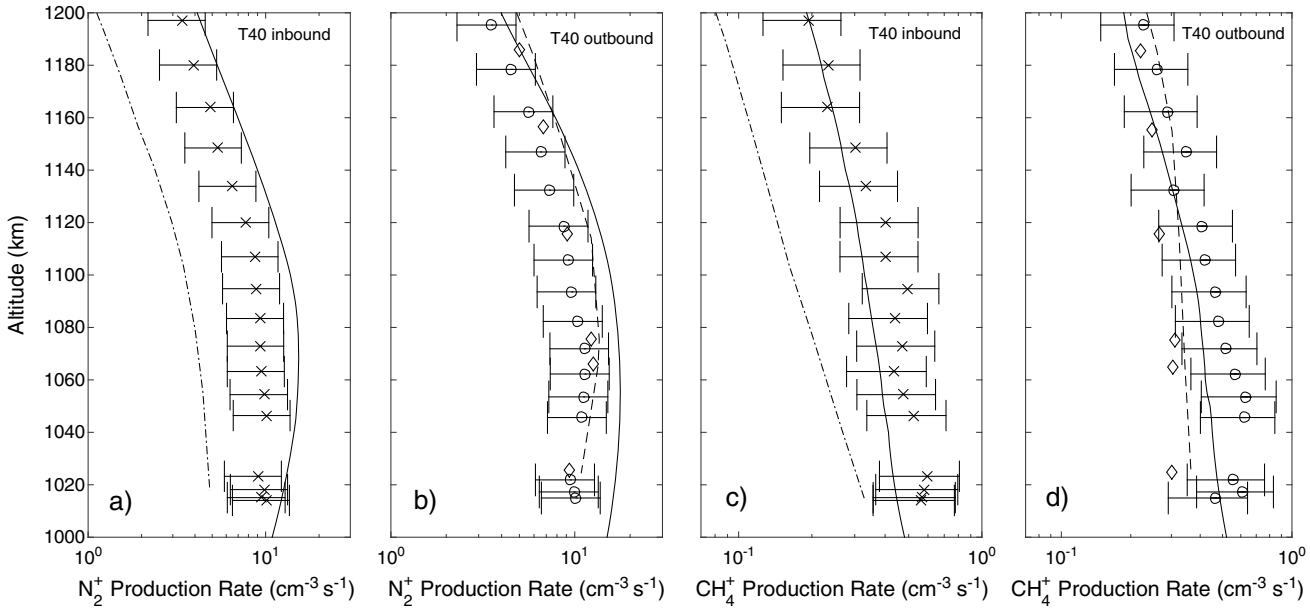

Figure 2. Comparison of production rates as a function of altitude from the chemical model (crosses and circles for inbound and outbound, respectively), from the solar energy deposition model (solid line), from the empirical and theoretical models of *Richard et al.* [2015a] (diamonds and dashed line, respectively), and from *Westlake et al.* [2012] (dash-dotted line). (a) N_2^+ for T40 inbound, (b) N_2^+ for T40 outbound, (c) CH_4^+ for T40 inbound, and (d) CH_4^+ for T40 outbound.

ionization frequency through equation (12) for short-lived ions and through equation (13) for long-lived ions. These relations are derived in Appendix A.

$$\log([A^+]) = \log(\nu_{A,A^+}) + \text{constant} \tag{12}$$

$$\log([F^+]) = \frac{1}{2}\log(\nu_{A,A^+}) + \text{constant} \tag{13}$$

Results from this ionospheric model are compared to the results from the chemical model in section 4.5.

3.6. Solar Illumination

As a measure of the amount of ionization possible, solar illumination is one of the parameters used to organize the data set. A point is said to be in darkness if the drop in solar radiation intensity from the top of the atmosphere as a result of photoabsorption is a factor greater than 1000 (in other words, if the optical depth is greater than about 7). A point is said to be under solar illumination if the drop in solar radiation intensity is less than 1000. The attenuation is evaluated at the HeII Lyman-α wavelength of 30.4 nm. The HeII Lyman-α wavelength is chosen as it is the line with the strongest solar intensity in the UV ionizing solar range. Choosing a smaller wavelength of 20 nm changes the total number of sunlit points by less than 5%. Decreasing the threshold intensity drop from 1000 to 100 lowered the total number of sunlit points by 7%, and doing so does not change any of the conclusions of this study discussed in section 4.

4. Results and Discussion

In section 4.1, the chemical model presented in section 3.1 is compared in terms of production rates of primary ions against the solar energy deposition model (see section 3.2) for flybys on Titan's dayside and against the ELS electron impact ionization model (see section 3.3) for flybys on Titan's nightside. In section 4.2, we look at the effect of local ionization on short-lived ions using the chemical model. In section 4.3, we discuss an interesting diurnal asymmetry in the behavior of the local ionization at Titan. In section 4.4, we look at the effect of local ionization on long-lived ions, as they are observed to behave very differently than short-lived ions. In section 4.5, we draw conclusions from an analysis including the short-lived and long-lived ions. Finally, in section 4.6, we compare our production rates of primary ions to previous publications.

4.1. Comparison of Production Models

4.1.1. Dayside Models

On Titan's dayside, solar radiation is the dominant source of ionization. Even though electron impact ionization from magnetospheric electrons is present on the dayside, it is overall negligible. It is therefore justified to compare the outputs of the chemical model (see section 3.1) to the ones from the solar energy deposition model (see section 3.2). Figure 2 compares the N_2^+ (Figures 2a and 2b) and CH_4^+ (Figures 2c and 2d) production rates derived from the chemical model (crosses and circles for inbound and outbound, respectively) and from the solar energy deposition (solid line) for T40 inbound (Figures 2a and 2c) and outbound (Figures 2b and 2d). For the two ion species, the shapes of the production rates are very similar between both models. However, the N_2^+ production rates from the solar energy deposition model are about two times higher than the ones from the chemical model, while the CH_4^+ production rate values are on the low side but agree within the uncertainties with those from the chemical model. The difference found in N_2^+ production rates and the agreement found in CH_4^+ production rates are observed for every dayside flyby that was analyzed.

The difference in N_2^+ production rate magnitude can come from several factors. First, the solar flux is expected to be known within 20% [*Woods et al.*, 2005] but has a larger uncertainty when extrapolated to Titan for large solar phase angles. However, if this were the source of the difference, there should also be a difference seen in CH_4^+ production rates, which is not the case. The Solar Dynamics Observatory (SDO) was not yet operational during the T40 flyby, but it was for T83 and T86 [*Woods et al.*, 2012]. For these flybys, the production rates were found to differ by less than 10% when using the solar flux from the SDO/EUV Variability Experiment instrument compared with TIMED/SEE. It is therefore not likely that this is the primary source of error.

Second, photoabsorption and photoionization cross sections below the ionization threshold are reported to be known within 3–5%, although stronger differences between data sets with different resolutions are found [*Fennelly and Torr*, 1992; *Shaw et al.*, 1992]. The importance of using high-resolution cross sections below the ionization threshold of N_2 has been highlighted. In that spectral range, autoionization is in competition with predissociation but this is still not fully characterized and might explain part of the difference in N_2^+ production rates [*Berkowitz*, 2002].

Third, INMS number densities have a systematic error of about 25% [*Teolis et al.*, 2015], but the shape of the production profiles agrees. Changing the neutral number densities significantly would affect the shape of the production profiles. A discussion of possible differences from a new neutral calibration factor is done in section 4.1.2.

Finally, it is also possible that the source of error is from the chemical model for the N_2^+ and CH_4^+ production rates in the factor coming from the exclusion of the minor reactions. However, comparisons of N_2^+ production rates between the chemical model and the ELS electron impact ionization model on the nightside (see section 4.1.2) show an overestimation from the chemical model of a factor from 2 to 3 for some flybys and having a larger correction factor would increase even more the overestimation of the chemical model.

The overestimation of the N_2^+ production rates from the solar energy deposition model is not new. It is reminiscent of the results found by *Vigren et al.* [2013], whose modeled electron number densities were larger by a factor of 2 than the ones obtained from the RPWS/LP instrument aboard Cassini. This implies a factor of 4 difference in electron production rates, assuming that the difference is purely due to production. The larger difference in electron density may be due to other missing loss processes or large uncertainties in some of the electron dissociative recombination rates. The cause is still under debate.

4.1.2. Nightside Models

Because electron impact ionization is expected to be the dominant source of ionization on Titan's nightside, the ELS electron impact ionization model is used to compare with the chemical model for nightside flybys. The N_2^+ production rates from both models (Figure 3, bottom) along with sample suprathermal electron spectra at around 1125 km (Figure 3, top) are shown for T5, T50, T57, and T59 from left to right, respectively, in Figure 3. There is a good agreement between both models in terms of the shape of the N_2^+ production rates; however, the chemical model overestimates the electron impact model by a factor of 2–3 for T5 and T59 while it is in better agreement for T50 and T57. While the former disagrees, the latter comparison is similar to what has been found by *Vigren et al.* [2015], where a good agreement of plasma number densities and short-lived ion densities between RPWS/LP and INMS/OSI observations and their model driven by a multiinstrumental Cassini data set was seen for nightside flybys.

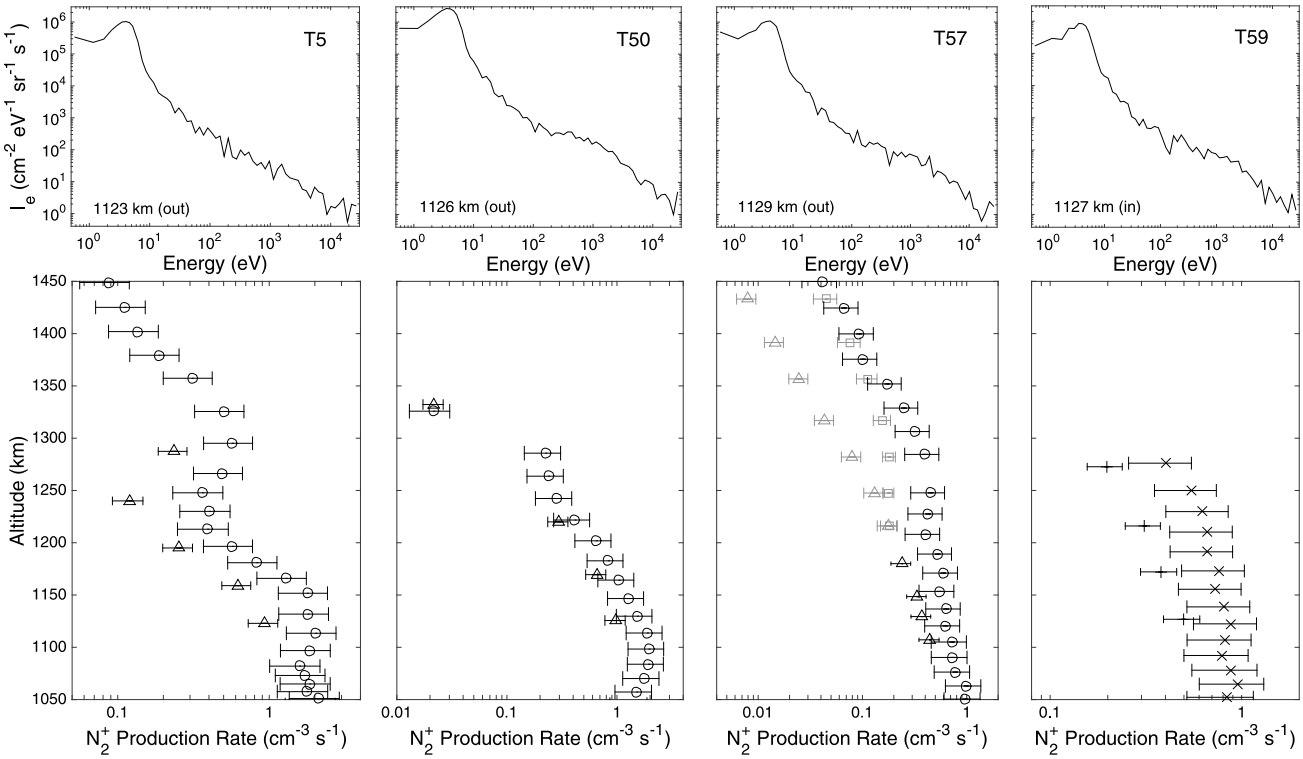

Figure 3. (top) CAPS/ELS electron intensity (I_e) spectra between 1120 and 1130 km for T5, T50, T57, and T59, from left to right, respectively. (bottom) Comparison of N_2^+ production rates as a function of altitude for T5, T50, T57, and T59, from left to right, respectively. Rates are derived from the chemical model (crosses and circles for inbound and outbound, respectively) and from the ELS electron impact model (pluses and triangles for inbound and outbound, respectively). The T57 outbound points in grey represent points that are under solar illumination. The T57 squares in grey are the same outbound points where the N_2^+ production from primary photoionization has been added.

It should be noted that T57 outbound above 1200 km corresponds to a region with SZA < 105°, that is, to a region under solar illumination as Titan has an extended atmosphere (see section 3.6). Primary photoionization therefore needs to be taken into account. If it is combined with electron impact ionization, as shown by the grey squares, the N_2^+ production rates for these T57 points increase to similar values as the ones from the chemical model.

As seen in Figure 3 (second column, top), the suprathermal electron intensity for T50 outbound at 1125 km is higher than for the other flybys. This results in large N_2^+ production rates for T50 (Figure 3, second column, bottom). T5 outbound has a high production rate similar to T50 at 1125 km although having similar electron intensities to T57 and T59. This is due to its N_2 number density being larger than the other three flybys by a factor of about 3. For CH_4^+, the production rates are not shown on the nightside because the signal-to-noise ratios of the CH_4^+ number densities observed by INMS are too low.

Finally, the effect of the new INMS calibration of the neutral densities needs to be discussed. In this study, a constant factor of 2.9 is adopted for neutral densities [*Koskinen et al.*, 2011; *Cui et al.*, 2012; *Westlake et al.*, 2012]. However, *Teolis et al.* [2015] suggested that the neutral calibration factor, varying with ram angle, azimuthal angle, and spacecraft speed, is closer to 2.2 for a ram angle of 0°, although it can be as small as 1.8 for an azimuthal angle of 180° and ram angle of 2°. As the ram angle of all data sets considered is below 2°, we have estimated the effect of a calibration factor for the neutral density between 1.8 and 2.2. Using this new calibration factor would reduce the production rates of both N_2^+ and CH_4^+ from the chemical model as well as from the ELS electron impact model by the same factor of 24–38% (see equations (1)–(3)). Therefore, the new neutral calibration factor would have no effect on our comparison of nightside production rates.

The solar energy deposition model, however, would be affected in a more complicated way. Both the optical depth and the number density of the the neutral population, which is ionized, would decrease. For a given altitude, the attenuated solar flux would be increased compared with the previous calibration. This yields a total decrease in production rates at the peak by at most 24% to 38%, depending on the azimuthal angle.

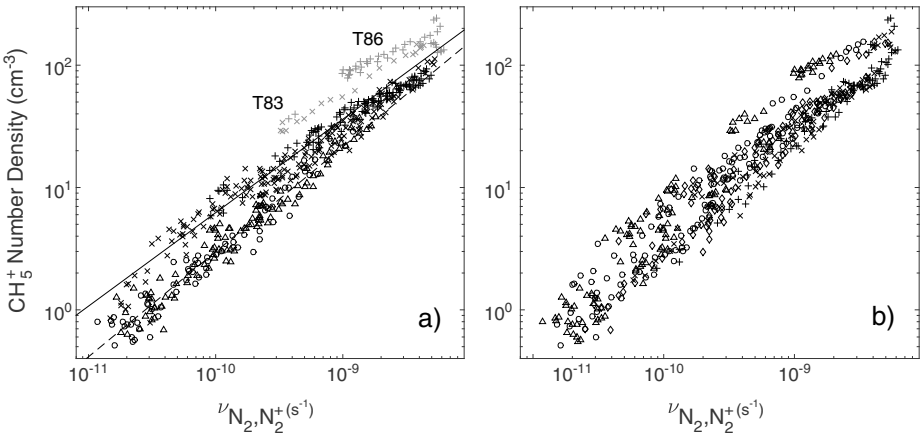

Figure 4. CH_5^+ number densities as a function of $N_2 \rightarrow N_2^+$ local ionization frequency for points from C/A to 1200 km for the 16 flybys. (a) The data set is organized by SZA: 0°–70° (pluses), 70°–105° (crosses), 105°–130° (circles), and 130°–180° (triangles). The solid line is a fit to points with SZA below 105°. The dashed line is a fit to points with SZA above 105°. Points associated with T83 and T86 are shown in dark grey and are included in the solid line fit. (b) The data set is organized by altitude: 1150–1200 km (pluses), 1100–1150 km (crosses), 1050–1100 km (diamonds), 1000–1050 km (circles), and <1000 km (triangles).

It would also decrease the peak altitude of the ion production rates derived from the solar energy deposition model by about 50 km, a peak altitude that is currently in agreement with the one from the chemical model (see Figure 3) and with the observed electron density from Cassini/RPWS/LP [*Vigren et al.*, 2013].

4.2. Short-Lived Ions

The chemical model is used to assess the effect of local ionization on the number densities of short-lived ions, those primarily lost through ion-neutral reactions with an associated chemical timescale of the order of 10^{-2} s or smaller [*Cui et al.*, 2009a]. For this purpose, the $N_2 \rightarrow N_2^+$ local ionization frequency, ν_{N_2,N_2^+}, defined in section 3.4, is used. From the ionospheric model described in section 3.5, short-lived ions are expected to show a strong positive correlation between their number density and the associated local ionization frequency. Furthermore, primary ions being produced solely from ionization of a neutral and lost only through an ion-neutral reaction (A^+ in section 3.5) are expected to witness a higher correlation than other short-lived ions being produced from an ion-neutral reaction (C^+ in section 3.5). In this section, we look at CH_5^+, $C_2H_3^+$, and $C_2H_5^+$ (analogous to ion C^+) to check whether a strong, positive correlation is found using the chemical model. The ions analyzed have been chosen for their relatively high signal-to-noise ratio. Figure 4 shows the CH_5^+ number density as a function of ν_{N_2,N_2^+} for points below 1200 km for the 16 flybys identified in Table 1. As anticipated, a clear, positive correlation is observed, emphasizing the strong influence of local ionization on the CH_5^+ number densities, where increased local ionization leads to higher CH_5^+ densities. This trend is observed for all of the short-lived ions analyzed.

There are, however, two flybys that stick out from the rest, T83 and T86, as shown in grey in Figure 4a. These two flybys occurred almost 2 years after the other flybys analyzed and correspond to the rising phase of Solar Cycle 24 [*Edberg et al.*, 2013]. The local ionization frequencies at the top of the atmosphere for these two flybys are therefore larger than for the other flybys. For T83 and T86, the INMS neutral data set shows that the neutral number densities at Titan are significantly lower than for the other flybys (a factor of 2 to 3 smaller than the average over all flybys at 1100 km). This is even more significant for CH_4, which witnesses an abnormally low volume mixing ratio (about 35% smaller than the average over all flybys at 1100 km). As the production and loss processes of CH_5^+ vary largely on the neutral number densities, a simple calculation of the effect of the amount of CH_4 for a given ν_{N_2,N_2^+} on CH_5^+ densities was made by assuming photochemical equilibrium of N_2^+, N_2H^+, and CH_5^+ and the chemical pathways of *Vuitton et al.* [2007]. Due to the smaller neutral number densities and the larger solar flux for these two flybys compared with the others, a given value of ν_{N_2,N_2^+} is reached at a lower altitude for these two flybys. At such lower altitudes, the CH_4 volume mixing ratio is significantly smaller than for the other flybys. The simple calculation shows that the different neutral background is most likely responsible for the increased CH_5^+ number density for a given ν_{N_2,N_2^+} witnessed at T83 and T86.

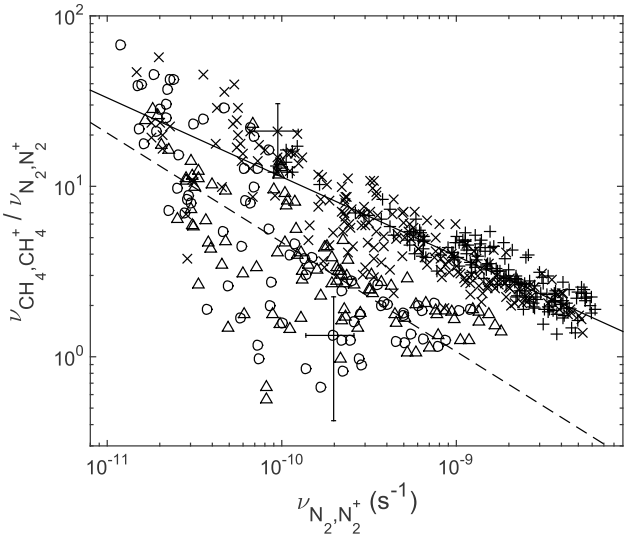

Figure 5. Ratio of $CH_4 \rightarrow CH_4^+$ to $N_2 \rightarrow N_2^+$ local ionization frequency from chemical model as a function of $N_2 \rightarrow N_2^+$ local ionization frequency for points from C/A to 1200 km for the 16 flybys. The data set is organized by SZA: 0°–70° (pluses), 70°–105° (crosses), 105°–130° (circles), and 130°–180° (triangles). The solid line is a fit to points with SZA below 105°. The dashed line is a fit to points with SZA above 105°. Example error bars are included for one dayside point and one nightside point.

In addition, CH_5^+ has an interesting characteristic that the other short-lived ion species analyzed do not show as clearly. The data set in Figure 4a is organized by SZA. A fit to all the points with an SZA below 105° (pluses and crosses) and a fit to those with an SZA above 105° (circles and triangles) are shown with a solid line and dashed line, respectively. The slopes of the fits are 0.76 and 0.86, respectively. Furthermore, there is a clear separation between dayside and nightside points, where points with smaller SZA have higher CH_5^+ number densities for a given ν_{N_2,N_2^+}. This can be explained by looking at the reactions leading to the production of CH_5^+. This ion is produced from two different chemical pathways, either from a reaction of CH_4^+ with CH_4 or from a series of reactions starting with N_2^+ [*Vuitton et al.*, 2007]. Our findings of SZA dependence imply that for the same ν_{N_2,N_2^+}, there is more ionization coming from the CH_4^+ pathway on the dayside than on the nightside. In other words, for the same ν_{N_2,N_2^+}, CH_4 is more efficiently ionized by solar radiation than by magnetospheric electrons. This behavior is further discussed in section 4.3. The fact that the slopes for the dayside and for the nightside are different is also explained by this behavior. As discussed in the following section, the relative efficiency of CH_4 ionization versus N_2 ionization observes an altitude dependence on the dayside which is not seen on the nightside. Figure 4b shows the same correlation for CH_5^+ as Figure 4a; however, the data set is organized by altitude. The high-altitude points (pluses and crosses representing 1100 to 1200 km) are at high ν_{N_2,N_2^+}. As ν_{N_2,N_2^+} decreases, the contribution of CH_5^+ coming from CH_4 increases on the dayside, due to its altitude dependence, but not on the nightside. This is what causes the widening gap between the dayside and nightside number densities for lower ν_{N_2,N_2^+}. The diurnal asymmetry and altitude dependence of the CH_4 ionization efficiency are discussed in more detail in section 4.3. A comparison of the results obtained here for short-lived ions to those from the ionospheric model is discussed in section 4.5.

4.3. Diurnal Asymmetry in Local Ionization Frequency

As discussed in section 4.2, the dependence of CH_5^+ number density as a function of ν_{N_2,N_2^+} exhibits interesting characteristics. More CH_5^+ is produced on the dayside than on the nightside, for the same ν_{N_2,N_2^+}. This implies that the $CH_4 \rightarrow CH_4^+$ pathway is more efficient on the dayside than on the nightside, for a given ν_{N_2,N_2^+}, keeping in mind that CH_5^+ originates from both CH_4 and N_2 ionization. To investigate this behavior, we compare ν_{N_2,N_2^+} and ν_{CH_4,CH_4^+}.

Figure 5 shows the $\nu_{CH_4,CH_4^+} / \nu_{N_2,N_2^+}$ ratio as a function of ν_{N_2,N_2^+} for the 16 flybys below 1200 km. This is done to characterize the response of the ratio of the ionization frequencies to local ionization (as measured by ν_{N_2,N_2^+}). As expected, for a given value of ν_{N_2,N_2^+}, dayside points with SZA < 105° (pluses and crosses) have a higher ratio than nightside points with SZA > 105° (circles and triangles). This is further shown by the solid line, a fit to dayside points (goodness of fit: 0.31), and the dashed line, a fit to nightside points (goodness of fit: 0.85). This means that for a given value of ν_{N_2,N_2^+} there is more CH_4 ionization on the dayside than on the nightside. The large spread witnessed for nightside points in Figure 5 is due to the low signal-to-noise ratio previously mentioned for CH_4^+ number densities derived from INMS.

In order to explain this finding, we have calculated the CH_4 to N_2 local ionization frequency ratio, $\nu_{CH_4,CH_4^+}/\nu_{N_2,N_2^+}$ (see section 3.4), using the solar energy deposition model (see section 3.2) and the ELS electron

Table 3. CH_4 to N_2 Ionization Frequency Ratio From Multiple Sources[a]

Source	Total Ratio	$CH_4 \rightarrow CH_4^+$ to $N_2 \rightarrow N_2^+$ Ratio
Schunk and Nagy [2009] solar minimum	1.72	-
Schunk and Nagy [2009] solar maximum	1.80	-
Solar energy deposition model	1.89	1.30
ELS electron impact model	-	0.86

[a] *Schunk and Nagy* [2009]: total ionization frequency ratio for solar maximum and solar minimum conditions at the top of the atmosphere (solar fluxes F79050N and F74133, respectively). Total ionization refers to ionization independent of the ion produced. Solar energy deposition model: both total CH_4 to N_2 ionization frequency ratio and $CH_4 \rightarrow CH_4^+$ to $N_2 \rightarrow N_2^+$ ionization frequency ratio from the average of values above 1300 km (optically thin atmosphere) from T40, T48, and T86. ELS model: $CH_4 \rightarrow CH_4^+$ to $N_2 \rightarrow N_2^+$ ionization frequency ratio from the average of every used spectra of the four flybys used (T5, T50, T57, and T59).

impact ionization model (see section 3.3). A summary of the various ratios obtained is shown in Table 3, along with the values obtained from *Schunk and Nagy* [2009] for solar minimum and solar maximum. The values for the solar energy deposition model use data from T40, T48, and T86 in the optically thin high-altitude region (>1300 km) while the ratio from the ELS electron impact model is an average of all the spectra of the four nightside flybys, T5, T50, T57, and T59. The total local ionization frequency ratio, independent of the ion produced, derived from the solar energy deposition model (total ratio of 1.89) agrees well with previous results from *Schunk and Nagy* [2009] (solar minimum and maximum values of 1.72 and 1.80, respectively). When calculating the ratio from the ELS model, an average value of 0.86 ± 0.07 is obtained. The fact that the ratio from the solar energy deposition model on the dayside (average value of 1.30 above 1300 km) is larger than the ratio from the ELS model on the nightside confirms that CH_4 is more efficiently ionized through photoionization than through electron impact ionization for a given value of ν_{N_2,N_2^+}.

Any INMS calibration updates on neutral densities (see section 2) would not affect the conclusions drawn here as we are comparing the ratios of local ionization frequencies at the top of the atmosphere. For the solar energy deposition model or the ELS electron impact model, the ionization frequencies are independent of the neutral densities (see equation (4)). For the chemical model, ν_{CH_4,CH_4^+} is independent of neutral number densities, and the calibration factor would cancel out in ν_{N_2,N_2^+} when taking the ratio of the neutral number densities (see equations (5) and (6)).

In addition, the local ionization ratio from the chemical model decreases with increasing ν_{N_2,N_2^+} for dayside points, as shown in Figure 5. This is due to the altitude dependence of the ratio. To get a better idea of how the local ionization ratio depends on altitude, Figure 6 displays the ν_{CH_4,CH_4^+} / ν_{N_2,N_2^+} local ionization frequency ratio as a function of altitude for points under solar illumination. There is a clear trend showing an increasing local ionization frequency ratio with decreasing altitude. To confirm these results, the same analysis was done using the solar energy deposition ratio. Figure 7 displays the ratio as a function of altitude from the solar energy deposition model for four dayside flybys, T18, T36, T48, and T86. The behavior found is the same as the one obtained from the chemical model. On the nightside, the ELS model provides a ratio which does not exhibit any altitude dependence.

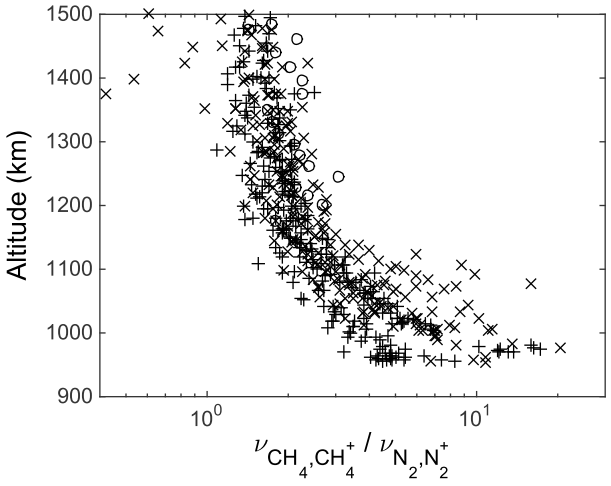

Figure 6. Ratio of $CH_4 \rightarrow CH_4^+$ to $N_2 \rightarrow N_2^+$ local ionization frequency from chemical model as a function of altitude for the 16 flybys. The data set is organized by SZA for points under solar illumination as defined in section 3.6: 0°–70° (pluses), 70°–105° (crosses), and 105°–130° (circles).

To better understand why there is this altitude dependence shown in Figures 6 and 7, we look at the effect of

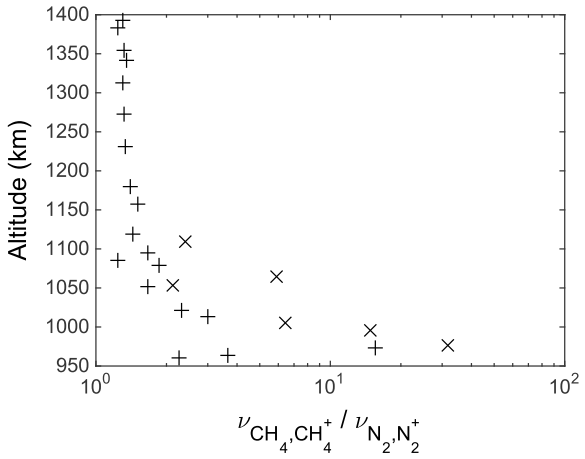

Figure 7. Ratio of $CH_4 \rightarrow CH_4^+$ to $N_2 \rightarrow N_2^+$ local ionization frequency from solar energy deposition model as a function of altitude for T18, T36, T40, T48, and T86. The data set is organized by SZA: 0°–70° (pluses) and 70°–105° (crosses).

the high-resolution N_2 photoabsorption cross sections on the ionization of CH_4 [*Lavvas et al.*, 2011; *Mandt et al.*, 2012]. Figure 8 displays the altitude at which the optical depth equals one, derived from the solar energy deposition model, as a function of wavelength for T40 outbound conditions at 60° SZA. The black line is obtained using low-resolution cross sections. The light grey and dark grey are from the *Shaw et al.* [1992] and CSE quantum mechanical model cross sections, respectively. The shape is very representative of and similarly structured to the N_2 photoabsorption cross sections [*Lewis et al.*, 2005, 2008a, 2008b]. Below 80 nm, CH_4 and N_2 have a very similar photoabsorption cross section structure; however, above 80 nm, CH_4 has a fairly constant photoabsorption cross section while N_2 is highly structured. If we look at what happens above 1300 km, where the atmosphere is optically thin, photons are absorbed and ionize at similar rates by both N_2 and CH_4, which explains the constant ratio above 1300 km in Figure 7. Below 1300 km, the relative contribution of N_2 and CH_4 ionization changes. Between the N_2 ionization threshold (80 nm) and the CH_4 ionization threshold (98 nm), only CH_4 is ionized. At the top of the atmosphere, this spectral range already accounts for more than 50% of the total CH_4^+ ionization. The highly structured N_2 photoabsorption cross sections mean that there are photons left to ionize CH_4 at some wavelengths at lower altitudes, increasing the relative contribution of CH_4 ionization compared to N_2 ionization, as part of the solar radiation below 80 nm is absorbed. The structure of the N_2 photoabsorption cross sections in the spectral region where CH_4, but not N_2, can be ionized (80–98 nm) is responsible for the altitude dependence of the local ionization frequency ratio and explains the increasing ratio with decreasing altitude, as illustrated in Figures 6 and 7. The analysis of *Lavvas et al.* [2011], which emphasized the importance of using high-resolution N_2 photoabsorption cross sections in the calculation of CH_4^+ production rates, predicts this finding and is verified by the observations found here. In the case of electron impact, the energy deposition is different, as unlike photons that are absorbed, suprathermal electrons are degraded in energy. Therefore, the important role played by the 80–98 nm spectral range in the CH_4 to N_2 ionization frequency ratio does not occur for electron impact processes.

4.4. Long-Lived Ions

A similar analysis to what was done in section 4.2 was done here for long-lived ions, which are defined as being primarily lost through electron dissociative recombination with a neutral [*Cui et al.*, 2009a]. As shown

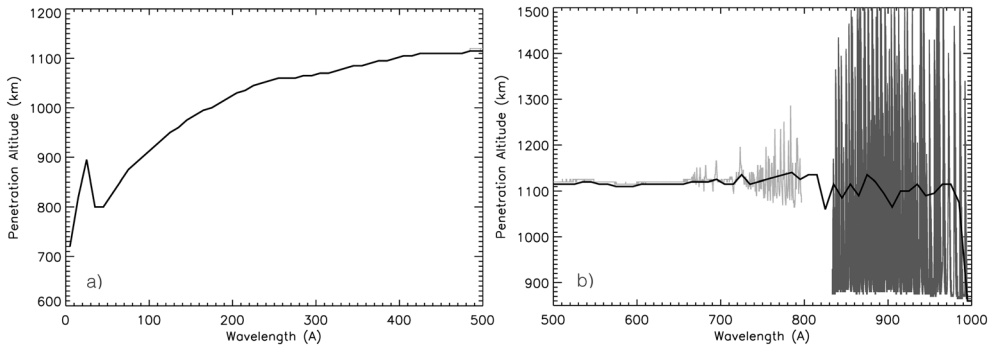

Figure 8. Photon penetration altitude at Titan as a function of wavelength from (a) 0 to 500 A and (b) 500 to 1000 A for T40 outbound conditions. The black line is from low-resolution cross sections. The light grey and dark grey are from *Shaw et al.* [1992] and from the CSE quantum mechanical model used by *Lavvas et al.* [2011], respectively.

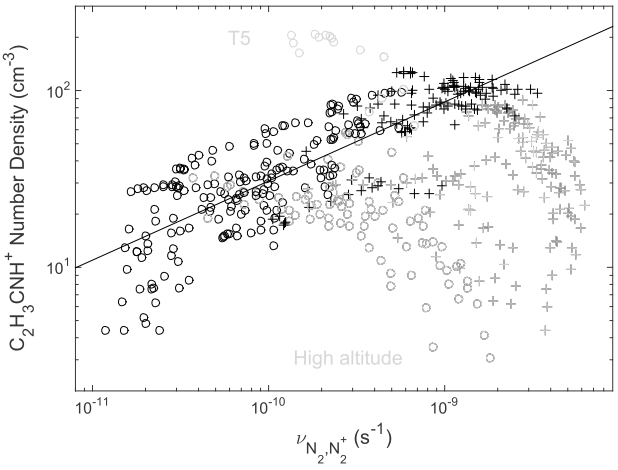

Figure 9. $C_2H_3CNH^+$ number density as a function of $N_2 \rightarrow N_2^+$ local ionization frequency for points from C/A to 1200 km for the 16 flybys. The data set is organized by solar illumination (see section 3.6): points which are under illumination (pluses) and points which are in darkness (circles). The solid line is a fit to all points, excluding points in grey which are from the T5 flyby or high-altitude points where the neutral number density is smaller than 5×10^9 cm^{-3}.

in section 3.5, the ionospheric model predicts that long-lived ions should demonstrate a positive but weaker correlation between their number density and the associated local ionization frequency than for short-lived ions. This was tested by looking at ions $HCNH^+$, NH_4^+, HC_3NH^+, $C_4H_3^+$, $C_2H_3CNH^+$, $C_6H_5^+$, and $C_7H_7^+$ (analogous to ion F^+ in section 3.5). Figure 9 shows the $C_2H_3CNH^+$ number density as a function of ν_{N_2,N_2^+} for points below 1200 km for all 16 flybys. There are several characteristics to the data set that need to be pointed out. The first is that T5, labeled at the top of the figure in light grey, witnesses unusually large number densities. At such a high mass (>50 amu), the transmission of the T5 INMS ion measurements is just above the cutoff of 0.5 (see section 2). With such a low transmission, the associated number densities should not be trusted. Most of the other points in the figure have a transmission above 0.8. Second, heavier ions, such as $C_2H_3CNH^+$, are harder to produce at higher altitudes due to the lower volume mixing ratio of heavy neutrals at higher altitudes, as a consequence of diffusive separation. The points that had a neutral number density smaller than 5×10^9 cm^{-3} (the average neutral number density of the 16 flybys at around 1100 km), represented in light grey in the bottom right of Figure 9, are therefore left out of the analysis for all of the heavy ions considered. It is worth noting that NH_4^+, which is a long-lived but light ion, does not display a significant reduction in number density at higher altitudes, as shown in Figure 10, which displays the NH_4^+ number density as a function of ν_{N_2,N_2^+}, similar to Figure 9 for $C_2H_3CNH^+$. However, the same neutral number density limit was adopted for consistency in the calculation of slope and goodness of fit.

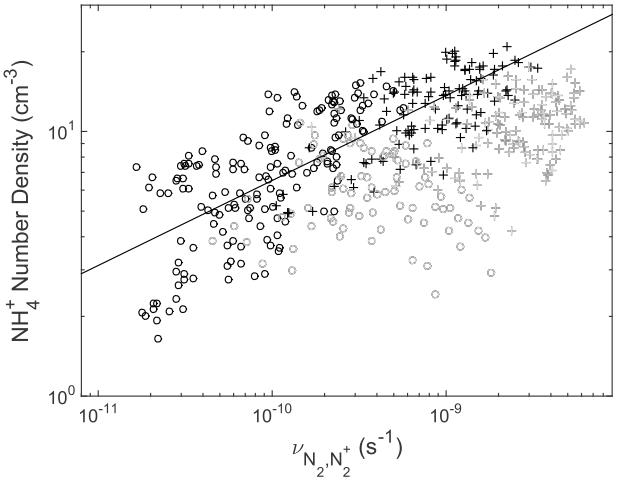

Figure 10. NH_4^+ number density as a function of $N_2 \rightarrow N_2^+$ local ionization frequency for points from C/A to 1200 km for the 16 flybys. The data set is organized by solar illumination (see section 3.6): points which are under illumination (pluses) and points which are in darkness (circles). The solid line is a fit to all points, excluding points in grey which are high-altitude points where the neutral number density is smaller than 5×10^9 cm^{-3}.

The data set (black symbols in Figure 9) is organized into points under solar illumination and points in darkness (see section 3.6). It shows, as expected, that the points under illumination are the ones that have higher ν_{N_2,N_2^+}, implying that overall ionization by electron precipitation is less important than ionization by solar radiation. The structured data set displays a positive correlation between local ionization and number density, as shown by the solid line fit. The slope of the fit for $C_2H_3CNH^+$ (0.45) is significantly smaller than the CH_5^+ slopes of 0.76 (dayside) and 0.86 (nightside). In addition, the spread with respect to the best fit functions is larger (goodness of fit: 0.44) than in the case of CH_5^+ (goodness of fit: 0.25 and 0.40 for nightside and dayside, respectively). Similar results are obtained for all of

Table 4. Results for the 10 Ions Analyzed[a]

Mass (amu)	Ion	γ	Goodness of Fit
17	CH_5^+	0.99 ± 0.02	0.49
18	NH_4^+	0.31 ± 0.01	0.34
27	$C_2H_3^+$	0.93 ± 0.02	0.40
28	$HCNH^+$	0.93 ± 0.01	0.25
29	$C_2H_5^+$	1.01 ± 0.01	0.29
51	$C_4H_3^+$	0.74 ± 0.01	0.35
52	HC_3CNH^+	0.62 ± 0.01	0.34
54	$C_2H_3CNH^+$	0.45 ± 0.02	0.44
77	$C_6H_5^+$	0.35 ± 0.02	0.45
91	$C_7H_7^+$	0.41 ± 0.02	0.54

[a]The slope γ and goodness of fit are calculated by including only points for which the neutral number density is greater than 5×10^9 cm^{-3}.

the other long-lived ions analyzed. Number densities of long-lived ions have therefore a significantly weaker dependence on local ionization and exhibit a larger spread compared with the case of short-lived ions. These findings can be explained as follows. Being lost through the slow electron recombination and produced after a chain of chemical reactions [*Vuitton et al.*, 2007], long-lived ions have densities which depend on earlier local production. In addition, as *Cui et al.* [2009a, 2010] have shown, transport may be an important source for long-lived ions. Such a process would increase the nightside densities independently of the local ionization.

4.5. All Ions

As described in sections 4.2 and 4.4, the slopes γ for short-lived ion CH_5^+ were 0.76 and 0.86 on the dayside and nightside, respectively, and for long-lived ion, $C_2H_3CNH^+$ was smaller with a value of 0.45. The slope γ corresponds to the slope of the linear fit to the logarithm of the ion density (in cm^{-3}) and the logarithm of ν_{N_2,N_2^+} (in s^{-1}). These values are consistent with theoretical calculations summarized in section 3.5 and derived in Appendix A. Assuming photochemical equilibrium and a loss through an ion-neutral reaction yields a slope of 1 (Case 1 presented in Appendix A). Allowing for time dependence provides a slope value of 0.92 for a short-lived, primary ion A^+ and 0.78 for a short-lived ion C^+, with C^+ being more representative of CH_5^+ [*Vuitton et al.*, 2007] (Case 3 in Appendix A). For long-lived ions lost through electron recombination, the ionospheric model provides an upper value of 0.5 for the slope γ (no time dependence, Case 2 in Appendix A) and a value of 0.31 when time dependence is taken into account (ion F^+, Case 3 in Appendix A). The consistency with the chemical results is discussed below.

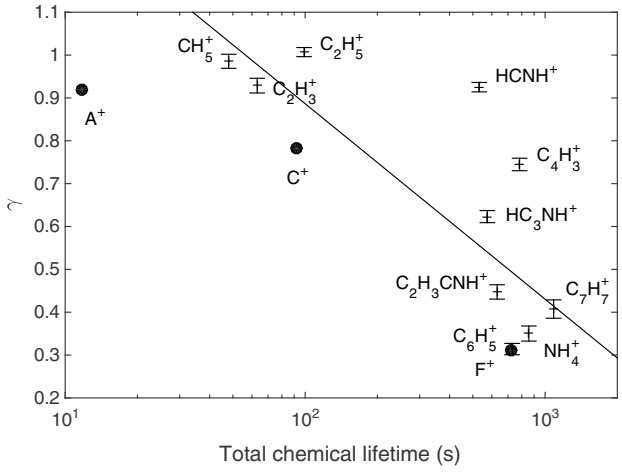

Figure 11. Slope γ as a function of the total ion chemical lifetime derived at 1050 km for the species analyzed (pluses with the vertical error bard representing the uncertainty on the slope) and the three ions from the analytical model (filled circles). The slope γ corresponds to the slope of the linear fit to the logarithm of the ion density (in cm^{-3}) and the logarithm of the $N_2 \rightarrow N_2^+$ local ionization frequency (in s^{-1}) for points with a neutral number density greater than 5×10^9 cm^{-3}.

An analysis of the slope γ was made for all the ions analyzed in sections 4.2 and 4.4. For consistency, γ was calculated for points with a neutral number density greater than 5×10^9 cm^{-3} for both the long-lived and short-lived ions. Table 4 shows the slopes and goodness of fit for the 10 ions analyzed. Only one value is shown for CH_5^+ as the difference in slope between

nightside and dayside disappears when only considering a short range of altitude points, although the spread between both data sets is still present, as shown by the large goodness of fit value (0.49).

In Figure 11, γ is organized as a function of the "total" chemical lifetime of the ion species. Since heavier ions are produced from a series of reactions and not directly from ionization of a neutral, the total chemical lifetime starting at the production of the primary ions is selected instead of the chemical lifetime only associated with the main loss process of the ion species. It is calculated by summing the chemical lifetime of all the ions involved in the chemical pathway forming the final ion from the initial ionization to the chemical loss of the final ion. This total chemical lifetime is a more accurate parameter for comparison than the chemical lifetime of individual ions when discussing local ionization as it provides a better link to the production of primary ions. The total lifetimes are calculated using the ionospheric model of *Vuitton et al.* [2007, 2009a] at 1050 km. For example, NH_4^+ is produced either from $HCNH^+$ or $C_2H_5^+$. The total chemical lifetime is obtained by adding the real chemical lifetime of NH_4^+, as calculated in a similar way to that found by *Cui et al.* [2009a], to the weighted average of the total chemical lifetimes of both $HCNH^+$ and $C_2H_5^+$. The two ions are weighed according to their contribution to the production rate of NH_4^+.

A trend is noticeable in Figure 11, suggesting that the ions with longer chemical lifetimes have a smaller slope. A fit to the logarithm of the chemical lifetime and γ provides a slope of -0.20 ± 0.05 with a goodness of fit of 0.25. This was calculated by excluding $HCNH^+$ due to the issues outlined below. The three filled circles in Figure 11 represent the output of the time-dependent ionospheric model for three typical ions, a primary A^+ and intermediate C^+ short-lived ion and a long-lived ion, F^+. The model output confirms that local ionization does have a strong impact on the initial short-lived ions and a decreasing impact on long-lived ions produced further down the ionospheric reaction chain, implying chemical survival of longer-lived ions, as previously suggested by *Cui et al.* [2009a].

An interesting result is the fact that the chemical lifetime of $HCNH^+$ is significantly larger than that of ions with similar γ. This behavior concurs with previously seen results in photochemical models that predicted too large $HCNH^+$ number densities compared with observations [e.g., *Vuitton et al.*, 2009a; *Robertson et al.*, 2009; *Mandt et al.*, 2012; *Westlake et al.*, 2012]. Furthermore, $C_4H_3^+$, a direct product of $HCNH^+$, also appears to have a large lifetime for its slope γ. A missing $HCNH^+$ loss process, as suggested by *Vuitton et al.* [2007] and *Westlake et al.* [2012], could explain these outlying points. A lower $HCNH^+$ lifetime would shift this ion toward the short-lived ions in Figure 11 and would also reduce significantly the total lifetime of $C_4H_3^+$, as production from $HCNH^+$ accounts for 56% of its total chemical lifetime. The other long-lived ions would not be affected as much as they are either further down the reaction chain, have relatively large individual chemical lifetimes, or are not as dependent on $HCNH^+$.

The INMS calibration updates mentioned in section 4.1 would have no significant impact on the discussion here as the values of v_{N_2,N_2^+} and v_{CH_4,CH_4^+} would remain unchanged (see equations (5) and (6)).

4.6. Comparison With Previous Work

The production rates obtained in this study have been compared to work that has previously been done by *Richard et al.* [2015a], *Westlake et al.* [2012], and *Vigren et al.* [2013]. As shown in Figure 2b, the N_2^+ production rates from the empirical model of *Richard et al.* [2015a] (diamonds) are similar to ours (circles), even though they do not include the 1.55 calibration factor on INMS ion number densities. Including this factor would increase their production rates (as shown by equation (1)) to similar values to our solar energy deposition model. The difference in our production rates could come from many factors. The reaction rate coefficients used by *Richard et al.* [2015a] are the same as those we use, and no significant difference was found between the CH_3^+ number densities of the two studies, other than the constant 1.55 calibration factor, so those two can be ruled out as potential sources of difference.

First, the correction factor that takes into account the effect of minor reactions could be a source of the difference; we use a factor of 1.35 compared to a factor of 1.49 in *Richard et al.* [2015a]. However, after adjusting our production rates to the altitude-dependent correction factor from *Richard et al.* [2015a], we found that these differences alter our production rates only slightly (<15%) and do not explain alone the large difference that has been found here.

Second, the CH_4 number densities used in both models are very different. The ones from *Richard et al.* [2015a] are about 50% larger than the ones used here obtained from *Cui et al.* [2012], which would increase their empirical production rates by the same amount.

Third, the solar-driven modeled production rates from *Richard et al.* [2015a] (dashed line) are also different from the ones in our solar energy-driven model (solid line). *Richard et al.* [2015a] show two different models using solar flux data from the solar EUV irradiance model for aeronomic cal- culations (EUVAC) and the Solar Irradiance Platform (SIP). However, *Richards et al.* [2006] point out that EUVAC underestimates terrestrial observations and needs to be adjusted upward at low wavelengths. We therefore only show the N_2^+ production rates that *Richard et al.* [2015a] obtained using the SIP solar flux, which are expected to roughly agree with TIMED/SEE values. Furthermore, *Richard et al.* [2015a] conclude that their use of EUVAC and SIP can only account for a 25% difference in modeled production rates.

Finally, it seems as though in Figure 2 of *Richard et al.* [2015a], the N_2 number densities from the global average model have been switched with the ones from T40 outbound. Indeed, our T40 outbound N_2 number density is about 5.4×10^9 cm^{-3} at 1100 km, while the N_2 number densities from *Richard et al.* [2015a] are approximately 5.5×10^9 cm^{-3} for the global average model and 4.0×10^9 cm^{-3} for the T40-labeled profile. If the neutral densities are switched, the lower neutral density values used by *Richard et al.* [2015a] compared to ours explain part of the difference found in terms of production rates. Furthermore, we speculate that the difference in neutral density between *Richard et al.* [2015a] and *Cui et al.* [2012] is related to different approaches of correcting for counter saturation in mass channels 16 and 28.

For the CH_4^+ production rates in Figure 2d, there is a good agreement between the empirical model from *Richard et al.* [2015a] (diamonds) and our chemical model (circles) if we take into account the fact that they did not include the calibration factor of 1.55. The correction factor we use to take into account minor reactions is a fixed 0.96, compared to a variable, altitude-dependent factor ranging from 0.5 to 0.9 from *Richard et al.* [2015a]. Their correction factor agrees well with our value above 1200 km; however, it becomes much smaller compared with ours at lower altitude, including at 1050 km, the altitude at which our calculation was explicitly done. By combining their lower correction factor and higher CH_4 number densities to our CH_4^+ number densities with the 1.55 calibration factor using equation (2), we obtained empirical CH_4^+ production rates similar to our default chemical profile which includes the saturation treatment of neutral densities. However, one would expect the theoretical values from *Richard et al.* [2015a] (dashed line) to be higher than ours (solid line), as their CH_4 number densities are much larger. This is not the case here, where similar lower production rates as the ones for N_2^+ are found at low altitudes. This might be due to their treatment of the high-resolution N_2 photoabsorption cross sections, which are approximated by assuming only 50% of photons interact with N_2 between 80 and 100 nm. This approach has not been properly validated against the work of *Lavvas et al.* [2011], and although it seems to work reasonably well for T40, such a method does not work for every flyby, especially at lower altitudes. Reproducing this technique was found to overproduce CH_4^+ primary production rates below 1000 km by an order of magnitude for T18 inbound and by almost a factor of 2 for T36 inbound. A detailed calculation as we have applied is therefore a more robust and suitable method to apply. With their different neutral number densities, a lower correction factor at low altitudes, and simplistic treatment of N_2 cross sections above 80 nm, *Richard et al.* [2015a] conclude that overproduction of primary ion species is not what is causing the discrepancies found between photochemical models and observations of electron and ion densities [e.g., *Vuitton et al.*, 2009a; *Robertson et al.*, 2009; *Westlake et al.*, 2012; *Mandt et al.*, 2012; *Vigren et al.*, 2013]. However, from our chemical and solar energy deposition models, we show that overproduction of N_2^+ is still an issue on the dayside.

We have also compared our N_2^+ and CH_4^+ production rates from T40 inbound to the ones from *Westlake et al.* [2012] (dash-dotted line in Figures 2b and 2d). However, from the much lower production rates and the decrease in peak altitude seen in the profiles of both ion production rates, it seems as though the calibration factor on neutral densities of the order of 3 used at the time has not been added. This is confirmed by comparing our neutral density profile with theirs from their Figure 4. At 1100 km, our T40 inbound N_2 number density is about 5×10^9 cm^{-3} compared to about 1.7×10^9 cm^{-3} from *Westlake et al.* [2012]. Using such underestimated values of neutral number densities has a significant impact on calculated ion production rates, as shown by the difference between profiles in Figure 2.

Finally, a comparison of total electron production rates obtained from the solar energy deposition model and the ones from *Vigren et al.* [2013], who use an energy deposition model developed independently from the one used here, shows a good agreement to within 10% at the peak altitude.

5. Summary

We have compared the chemical model proposed based on INMS ion and neutral number densities (see section 3.1) to a solar energy deposition model (see section 3.2) for dayside flybys and to an electron impact ionization model (see section 3.3) for nightside flybys (see section 4.1). On the dayside, the chemical model reproduces the shape of the production rates very well, although the N_2^+ production rates from the chemical model are smaller by a factor of 2 than the solar energy deposition model. On the nightside, the chemical model underestimates the N_2^+ production rates by a factor of 2–3 for some flybys while being in a better agreement for others. Regarding CH_4^+ production rates compared on the dayside, the agreement between the two models is very good in terms of both shape and magnitude. In contrast to *Richard et al.* [2015a], who concluded that the production of primary ions is well understood, the overproduction of N_2^+ found here suggests that there is still a problem with the models, the cause of which is still an open question.

Short-lived (see section 4.2) and long-lived ions (see section 4.4) are found to react differently to local ionization. A strong positive correlation between ion number density and local ionization frequency was derived for short-lived ions, and this trend was found to get weaker as the total chemical lifetime of the ion increased (see section 4.5). Modeling work presented in section 3.5 and Appendix A on the dependence of ion density on local ionization frequency supports these findings. This also confirms, as *Cui et al.* [2009a] first reported, that chemical survival is driving longer-lived ion densities, making them more weakly correlated to local ionization sources. Nevertheless, the behavior of some ions is still unexplained. $HCNH^+$ witnessed a correlation stronger than what would be anticipated for its total chemical lifetime. A possible explanation is missing loss processes, as previously suggested by *Vuitton et al.* [2007] and *Westlake et al.* [2012], who found that the $HCNH^+$ number densities from their photochemical models were too high compared to INMS observations. The overproduction of electrons on the dayside found by *Vigren et al.* [2013] is consistent with the overproduction of N_2^+ by energy deposition models and the missing key loss processes.

The analysis of local ionization frequency has shown that points under solar illumination had higher $N_2 \rightarrow N_2^+$ local ionization frequencies than the ones in darkness, confirming previous results that at the altitude region analyzed (950–1200 km) electron impact is a minor source of ionization compared to the absorption of solar UV radiation [e.g., *Cravens et al.*, 2009; *Galand et al.*, 2010; *Vigren et al.*, 2013]. Moreover, CH_5^+ was seen to display an interesting diurnal asymmetry that has not previously been mentioned in the literature. For the same $N_2 \rightarrow N_2^+$ local ionization frequency, higher CH_5^+ number densities were found for points on the dayside than on the nightside. This was demonstrated to be due to CH_4 being more efficiently ionized from photoionization than from electron impact ionization. A comparison to the solar energy deposition model and ELS electron impact ionization model confirmed this result. The chemical model and solar energy deposition model also displayed an altitude dependence in the $CH_4 \rightarrow CH_4^+$ to $N_2 \rightarrow N_2^+$ local ionization frequency ratio. We concluded that the ratio increased with decreasing altitude due to the highly structured N_2 photoabsorption cross sections between N_2 and CH_4 ionization thresholds (80–98 nm) which led to an increasing relative contribution of CH_4 ionization at lower altitudes, as predicted by *Lavvas et al.* [2011]. Overall, it was shown that the N_2 to N_2^+ local ionization frequency calculated from the chemical model is a reliable and easy tracer of local ionization. In addition, it can be used to obtain a quick estimate of the ionospheric densities, especially for short-lived ions below 1200 km.

Appendix A

Case 1: Short-lived, primary ion A^+ with no time dependence. We look at short-lived primary ions, such as A^+, that are produced from photoionization or electron impact ionization (reaction (7)) and that are lost only through an ion-neutral reaction (reaction (8)). In order to obtain a relationship between the number density of A^+ and the ionization frequency ν_{A,A^+} at a given altitude, we assume photochemical equilibrium:

$$P_{A^+} = L_{A^+} \tag{A1}$$

$$\nu_{A,A^+}[A] = k_{A^+,B}[A^+][B] \tag{A2}$$

where $k_{A^+,B}$ is the reaction rate coefficient for reaction (8). That is,

$$[A^+] = \frac{[A]}{k_{A^+,B}[B]}\nu_{A,A^+} \tag{A3}$$

$$\log([A^+]) = \log(\nu_{A,A^+}) + \text{constant} \tag{A4}$$

The slope γ, defined between $\log(\nu_{A,A^+})$ and $\log([A^+])$ (see section 4.5), for such an ion is therefore 1 when ignoring time dependence. However, the constant in equation (A4) is altitude dependent as it is a function of the neutral densities of both species A and B. Nevertheless, having a large sample size that is spread evenly in the ratio of the number densities of A to B across the altitude range considered, as we assume to have with the 16 flybys considered in this study, would conserve the slope γ. It is therefore not surprising that the short-lived ions in Figure 11 have slopes close to 1.

Case 2: Long-lived ion F^+ with no time dependence. The second case is one where an ion is produced from an ion-neutral reaction, lost only through electron recombination and where the time dependence is still neglected. This would be the case of ion F^+ in reactions (9) and (11). If we ignore reaction (10), assume photochemical equilibrium at a given altitude and naming α_{F^+}, the electron recombination rate coefficient for reaction (11):

$$P_{A^+} = L_{A^+} = P_{C^+} = L_{C^+} = P_{F^+} = L_{F^+} \tag{A5}$$

$$\nu_{A,A^+}[A] = \alpha_{F^+}[F^+][e^-] \tag{A6}$$

We introduce a mean recombination rate over all ion species i, $\bar{\alpha}$, and a mean local ionization frequency over all neutral species n, $\bar{\nu}$, defined as follows:

$$\bar{\alpha} = \frac{\Sigma_i \alpha_i[i]}{\Sigma_i[i]} = \frac{\Sigma_i \alpha_i[i]}{[e^-]} \tag{A7}$$

$$\bar{\nu} = \frac{\Sigma_n \nu_n[n]}{\Sigma_n[n]} = \frac{\Sigma_n \nu_n[n]}{[n_{tot}]} \tag{A8}$$

where $[n_{tot}]$ is the total number density. The expression for electron number density is as follows:

$$[e^-] = \frac{\Sigma_n \nu_n[n]}{\Sigma_i \alpha_i[i]} \tag{A9}$$

Equations (A7) and (A8) imply

$$[e^-] = \frac{\bar{\nu}[n_{tot}]}{\bar{\alpha}[e^-]} \tag{A10}$$

That is,

$$[e^-] = \sqrt{\frac{\bar{\nu}[n_{tot}]}{\bar{\alpha}}} \tag{A11}$$

If we also assume that atmospheric composition and ionospheric processes do not change with the local ionization frequency, then ν_{A,A^+} is proportional to $\bar{\nu}$: $\nu_{A,A^+} = \bar{\nu} C_{A,A^+}$. As a result, equation (A6) becomes

$$[F^+] = \frac{\mu_A \sqrt{\bar{\alpha}[k_{tot}] C_{A,A^+}}}{\alpha_{F^+}} \sqrt{\nu_{A,A^+}} \tag{A12}$$

where μ_A is the volume mixing ratio of A. That is,

$$\log([F^+]) = \frac{1}{2}\log(\nu_{A,A^+}) + \text{constant} \tag{A13}$$

In this case, the slope γ for such an ion is 0.5 when ignoring time dependence. This explains the behavior of some of the long-lived ions lost mostly through electron recombination in Figure 11. Some of the long-lived ions have even smaller slopes. This is due to the time dependence that has so far been neglected.

Case 3: Time dependence calculation for A^+, C^+, and F^+. To get a more realistic view, time dependence is included and its effect on the relationship between local ionization frequency and ion density is assessed. The continuity equations for ions A^+, C^+, and F^+ were solved analytically at altitudes from 950 to 1200 km every 50 km assuming reactions (7)–(11). The solar flux and neutral densities of T40 inbound were used. The neutral densities were assumed to be constant with time, and the time dependence of the local ionization frequency from solar radiation was calculated at an approximate T40 latitude of −10° and the T40 subsolar latitude of −8.8°. A background local ionization frequency of 10^{-11} s^{-1} was included to simulate electron impact ionization on the nightside. Typical values for the reaction rates were taken from *Vuitton et al.* [2007]. $k_{A^+,B}$ and $k_{C^+,E}$ were taken to be 10^{-9} cm^3 s^{-1} and 6×10^{-9} cm^3 s^{-1}, respectively. N_2 was used for neutral A, CH_4 for B, and C_2H_4 for E, set as 1% of the CH_4 number density. α_{C+}, α_{F+}, and $\bar{\alpha}$ were taken to be 4×10^{-7} cm^3 s^{-1}, 10^{-7} cm^3 s^{-1}, and 10^{-7} cm^3 s^{-1}, respectively. The factor C_A was set to 50% to represent the approximate fraction of ν_{N_2,N_2^+} to $\bar{\nu}$.

The values of the slope γ and total chemical lifetime obtained for the three ions are plotted in Figure 11 as filled circles. The total chemical lifetime was calculated at 1050 km in the same way as explained in section 4.5. The slope γ was calculated by including the analytical solutions at every altitude grid point. The short-lived, primary ion A^+ has a slope of 0.92, comparable to the slopes of some of the short-lived ions analyzed. The ion C^+, which is partially lost through electron recombination (similarly to CH_5^+), has a slope of 0.78, emphasizing the departure from the A^+ case as a result of the influence of electron recombination. Finally, the slope for the long-lived ion F^+ only lost by electron recombination, like $C_2H_3CNH^+$, is 0.31, which is smaller than the expected 0.5 if time dependence is excluded. The finding for long-lived ions is in agreement with those derived empirically as illustrated in Figure 11. The values of γ were found to be strongly dependent on the different reaction rate coefficients. They are also sensitive to the set of altitude and SZA considered. The values provided here for γ should be considered as an illustration of the trend between primary and intermediate short-lived and long-lived ions, with γ decreasing with lifetime.

Acknowledgments

L.S. and M.G. are partially funded by STFC through the consolidated grant to Imperial College London. L.S. would also like to thank the Royal Astronomical Society and the Imperial College Trust for their financial support. J.C. acknowledges support from the National Science Foundation of China (NSFC) through grants 41174146 and 41374178. E.V. is grateful for funding from the Swedish Research Council (contract 2011-894) and from the Swedish National Space Board. Support for this work was provided by a Centre National d'Etudes Spatiales Cassini Participating Scientist grant (to V.V.). A.J.C. and A.W. acknowledge support via the UCL-MSSL consolidated grant from STFC, UK. We thank the TIMED/SEE PI, Tom Woods, and his team for providing us with the solar flux data set and associated routines of extrapolation to planets. The Cassini INMS data analyzed in this paper were obtained from the NASA Planetary Data System (PDS) public archives. The CAPS/ELS data were provided from the lead Co-I of the experiment, Andrew Coates.

References

Ågren, K., J.-E. Wahlund, P. Garnier, R. Modolo, J. Cui, M. Galand, and I. Müller-Wodarg (2009), On the ionospheric structure of Titan, *Planet. Space Sci.*, *57*, 1821–1827, doi:10.1016/j.pss.2009.04.012.

Ågren, K., N. J. T. Edberg, and J.-E. Wahlund (2012), Detection of negative ions in the deep ionosphere of Titan during the Cassini T70 flyby, *Geophys. Res. Lett.*, *39*, L10201, doi:10.1029/2012GL051714.

Berkowitz, J. (2002), *Atomic and Molecular Photoabsorption: Absolute Total Cross Sections*, Academic Press, San Diego, Calif.

Bird, M. K., R. Dutta-Roy, S. W. Asmar, and T. A. Rebold (1997), Detection of Titan's ionosphere from Voyager 1 radio occultation observations, *Icarus*, *130*, 426–436, doi:10.1006/icar.1997.5831.

Coates, A. J., F. J. Crary, G. R. Lewis, D. T. Young, J. H. Waite, and E. C. Sittler (2007), Discovery of heavy negative ions in Titan's ionosphere, *Geophys. Res. Lett.*, *34*, L22103, doi:10.1029/2007GL030978.

Coates, A. J., A. Wellbrock, G. R. Lewis, G. H. Jones, D. T. Young, F. J. Crary, and J. H. Waite Jr. (2009), Heavy negative ions in Titan's ionosphere: Altitude and latitude dependence, *Planet. Space Sci.*, *57*, 1866–1871, doi:10.1016/j.pss.2009.05.009.

Crary, F. J., B. A. Magee, K. Mandt, J. H. Waite, J. Westlake, and D. T. Young (2009), Heavy ions, temperatures and winds in Titan's ionosphere: Combined Cassini CAPS and INMS observations, *Planet. Space Sci.*, *57*, 1847–1856, doi:10.1016/j.pss.2009.09.006.

Cravens, T. E., et al. (2006), Composition of Titan's ionosphere, *Geophys. Res. Lett.*, *33*, L07105, doi:10.1029/2005GL025575.

Cravens, T. E., et al. (2009), Model-data comparisons for Titan's nightside ionosphere, *Icarus*, *199*, 174–188, doi:10.1016/j.icarus.2008.09.005.

Cravens, T. E., et al. (2010), Dynamical and magnetic field time constants for Titan's ionosphere: Empirical estimates and comparisons with Venus, *J. Geophys. Res.*, *115*, A08319, doi:10.1029/2009JA015050.

Cui, J., M. Galand, R. V. Yelle, V. Vuitton, J.-E. Wahlund, P. P. Lavvas, I. C. F. Müller-Wodarg, T. E. Cravens, W. T. Kasprzak, and J. H. Waite Jr. (2009a), Diurnal variations of Titan's ionosphere, *J. Geophys. Res.*, *114*, A06310, doi:10.1029/2009JA014228.

Cui, J., et al. (2009b), Analysis of Titan's neutral upper atmosphere from Cassini Ion Neutral Mass Spectrometer measurements, *Icarus*, *200*, 581–615, doi:10.1016/j.icarus.2008.12.005.

Cui, J., M. Galand, R. V. Yelle, J. Wahlund, K. Ågren, J. H. Waite, and M. K. Dougherty (2010), Ion transport in Titan's upper atmosphere, *J. Geophys. Res.*, *115*, A06314, doi:10.1029/2009JA014563.

Cui, J., R. V. Yelle, D. F. Strobel, I. C. F. Müller-Wodarg, D. S. Snowden, T. T. Koskinen, and M. Galand (2012), The CH^4 structure in Titan's upper atmosphere revisited, *J. Geophys. Res.*, *117*, E11006, doi:10.1029/2012JE004222.

Curdt, W., D. Germerott, K. Wilhelm, U. Schühle, L. Teriaca, D. Innes, K. Bocchialini, and P. Lemaire (2013), The SUMER data in the SOHO archive, *Sol. Phys.*, *289*, 2345–2376, doi:10.1007/s11207-013-0449-7.

Dutuit, O. et al. (2013), Critical review of N, N^+, N_2^+, N^{++}, and N_2^{++} main production processes and reactions of relevance in Titan's atmosphere, *Astrophys. J. Suppl. Ser.*, *204*, 20, doi:10.1088/0067-0049/204/2/20.

Edberg, N. J. T., D. J. Andrews, O. Shebanits, K. Ågren, J.-E. Wahlund, H. J. Opgenoorth, T. E. Cravens, and Z. Girazian (2013), Solar cycle modulation of Titan's ionosphere, *J. Geophys. Res. Space Physics*, *118*, 5255–5264, doi:10.1002/jgra.50463.

Fennelly, J. A., and D. G. Torr (1992), Photoionization and photoabsorption cross sections O, N_2, O_2, and N for aeronomic calculations, *At. Data Nucl. Data Tables*, *51*, 321–363.

Galand, M., R. Yelle, J. Cui, J. -E. Wahlund, V. Vuitton, A. Wellbrock, and A. Coates (2010), Ionization sources in Titan's deep ionosphere, *J. Geophys. Res.*, *115*, A07312, doi:10.1029/2009JA015100.

Gronoff, G., J. Lilensten, and R. Modolo (2009), Ionization processes in the atmosphere of Titan II. Electron precipitation along magnetic field lines, *Astron. Astrophys.*, *506*, 965–970, doi:10.1051/0004-6361/200912125.

Kliore, A. J., A. F. Nagy, T. E. Cravens, M. S. Richard, and A. M. Rymer (2011), Unusual electron density profiles observed by Cassini radio occultations in Titan's ionosphere: Effects of enhanced magnetospheric electron precipitation?, *J. Geophys. Res.*, *116*, A11318, doi:10.1029/2011JA016694.

Koskinen, T. T., R. V. Yelle, D. S. Snowden, P. Lavvas, B. R. Sandel, F. J. Capalbo, Y. Benilan, and R. A. West (2011), The mesosphere and thermosphere of Titan revealed by Cassini/UVIS stellar occultations, *Icarus*, *216*, 507–534, doi:10.1016/j.icarus.2011.09.022.

Lavvas, P., M. Galand, R. V. Yelle, A. N. Heays, B. R. Lewis, G. R. Lewis, and A. J. Coates (2011), Energy deposition and primary chemical products in Titan's upper atmosphere, *Icarus*, *213*, 233–251, doi:10.1016/j.icarus.2011.03.001.

Lavvas, P., et al. (2013), Aerosol growth in Titan's ionosphere, *Proc. Natl. Acad. Sci.*, *110*, 2729–2734, doi:10.1073/pnas.1217059110.

Lewis, B. R., S. T. Gibson, W. Zhang, H. Lefebvre-Brion, and J. -M. Robbe (2005), Predissociation mechanism for the lowest $^1\Pi_u$ states of N_2, *J. Chem. Phys.*, *122*, 144,302–144,311.

Lewis, B. R., A. N. Heays, S. T. Gibson, H. Lefebvre-Brion, and R. Lefebvre (2008a), A coupled-channel model of the $^3\Pi_u$ states of N_2: Structure and interactions of the $3s\sigma_g F_3^3\Pi_u$ and $3p\pi_u G_3^3\Pi_u$ Rydberg states, *J. Chem. Phys.*, *129*, 164,306–164,315.

Lewis, G. R., K. G. H. Baldwin, A. N. Heays, S. T. Gibson, J. P. Sprengers, W. Ubachs, and M. Fujitake (2008b), Structure and predissociation of the $3p\sigma_u D^3\Sigma_u^+$ Rydberg state of N_2: First extreme-ultraviolet and new near-infrared observations, with coupled-channels analysis, *J. Chem. Phys.*, *129*, 204,303–204,314.

Lewis, G. R., et al. (2010), The calibration of the Cassini-Huygens CAPS electron spectrometer, *Planet. Space Sci.*, *58*, 427–436, doi:10.1016/j.pss.2009.11.008.

Liu, X., and D. E. Shemansky (2006), Analysis of electron impact ionization properties of methane, *J. Geophys. Res.*, *111*, A04303, doi:10.1029/2005JA011454.

Ma, Y., A. F. Nagy, T. E. Cravens, I. V. Sokolov, K. C. Hansen, J. Wahlund, F. J. Crary, A. J. Coates, and M. K. Dougherty (2006), Comparisons between MHD model calculations and observations of Cassini flybys of Titan, *J. Geophys. Res.*, *111*, A05207, doi:10.1029/2005JA011481.

Magee, B. A., J. H. Waite, K. E. Mand, J. Westlake, J. Bell, and D. A. Gell (2009), INMS-derived composition of Titan's upper atmosphere: Analysis methods and model comparison, *Planet. Space Sci.*, *57*, 1895–1916, doi:10.1016/j.pss.2009.06.016.

Mandt, K. E., et al. (2012), Ion densities and composition of Titan's upper atmosphere derived from the Cassini Ion Neutral Mass Spectrometer: Analysis methods and comparison of measured ion densities to photochemical model simulations, *J. Geophys. Res.*, *117*, E10006, doi:10.1029/2012JE004139.

McEwan, M. J., and V. G. Anicich (2007), Titan's ion chemistry: A laboratory perspective, *Mass Spectrom. Rev.*, *26*, 281–319, doi:10.1002/mas.20117.

Peterson, J. R. et al. (1998), Dissociative recombination and excitation of N_2^+: Cross sections and product branching ratios, *J. Chem. Phys.*, *108*, 1978–1988, doi:10.1063/1.475577.

Richard, M. S., et al. (2015a), An empirical approach to modeling ion production rates in Titan's ionosphere I: Ion production rates on the dayside and globally, *J. Geophys. Res. Space Physics*, *120*, 1264–1280, doi:10.1002/2013JA019706.

Richard, M. S., et al. (2015b), An empirical approach to modeling ion production rates in Titan's ionosphere II: Ion production rates on the nightside, *J. Geophys. Res. Space Physics*, *120*, 1281–1298, doi:10.1002/2014JA020343.

Richards, P. G., T. N. Woods, and W. K. Peterson (2006), HEUVAC: A new high resolution solar EUV proxy model, *Adv. Space Res.*, *37*, 315–322, doi:10.1016/j.asr.2005.06.031.

Robertson, I. P., et al. (2009), Structure of Titan's ionosphere: Model comparisons with Cassini data, *Planet. Space Sci.*, *57*, 1834–1846, doi:10.1016/j.pss.2009.07.011.

Samson, J. A. R., G. N. Haddad, T. Masuoka, P. N. Pareek, and D. A. L. Kilcoyne (1989), Ionization yields, total absorption, and dissociative photoionization cross sections of CH_4 from 110 to 950 Å, *J. Chem. Phys.*, *90*, 6925–6932, doi:10.1063/1.456267.

Schunk, R. W., and A. F. Nagy (2009), *Ionospheres: Physics, Plasma Physics, and Chemistry*, 2nd ed., Cambridge Univ. Press, Cambridge, U. K.

Shaw, D. A., D. M. P. Holland, M. A. MacDonald, A. Hopkirk, M. A. Hayes, and S. M. McSweeney (1992), A study of the absolute photoabsorption cross section and the photoionization quantum efficiency of nitrogen from the ionization threshold to 485 Å, *Chem. Phys.*, *166*, 379–391.

Shebanits, O., J.-E. Wahlund, K. Mandt, K. Ågren, N. Edberg, and J. H. Waite Jr. (2013), Negative ion densities in the ionosphere of Titan-Cassini RPWS/LP results, *Planet. Space. Sci.*, *84*, 153–162, doi:10.1016/j.pss.2013.05.021.

Shemansky, D. E., and X. Liu (2005), Evaluation of electron impact excitation of N_2 $X^1\Sigma_g^+(0)$ into the N_2^+ $X^2\Sigma_g^+(v)$, $A^2\Pi_u(v)$, and $B^2\Sigma_u^+(v)$ states, *J. Geophys. Res.*, *110*, A07307, doi:10.1029/2005JA011062.

Stolte, W. C., Z. X. He, J. N. Cutler, Y. Lu, and J. A. R. Samson (1998), Dissociative photoionization cross sections of N_2 and O_2 from 100 to 800 eV, *At. Data Nucl. Data Tables*, *69*, 171–179.

Teolis, B. D., et al. (2015), A revised sensitivity model for Cassini INMS: Results at Titan, *Space Sci. Rev.*, *186*, 1–38, doi:10.1007/s11214-014-0133-8.

Thomas, R. D., et al. (2012), Dissociative recombination of vibrationally cold CH_3^+ and interstellar implications, *Astrophys. J.*, *758*, 55, doi:10.1088/0004-637X/758/1/55.

Vigren, E., et al. (2013), On the thermal electron balance in Titan's sunlit upper atmosphere, *Icarus*, *223*, 234–251, doi:10.1016/j.icarus.2012.12.010.

Vigren, E., M. Galand, O. Shebanits, J.-E. Wahlund, W. D. Geppert, P. Lavvas, V. Vuitton, and R. V. Yelle (2014), Increasing positive ion number densities below the peak of ion-electron pair production in Titan's ionosphere, *Astrophys. J.*, *786*, 69, doi:10.1088/0004-637X/786/1/69.

Vigren, E., et al. (2015), Ionization balance in Titan's nightside ionosphere, *Icarus*, *248*, 539–546, doi:10.1016/j.icarus.2014.11.012.

Vuitton, V., R. V. Yelle, and V. G. Anicich (2006), The nitrogen chemistry of Titan's upper atmosphere revealed, *Astrophys. J.*, *647*, L175–L178.

Vuitton, V., R. V. Yelle, and M. J. McEwan (2007), Ion chemistry and N-containing molecules in Titan's upper atmosphere, *Icarus*, *191*, 722–742.

Vuitton, V., R. V. Yelle, and J. Cui (2008), Formation and distribution of benzene on Titan, *J. Geophys. Res.*, *113*, E05007, doi:10.1029/2007JE002997.

Vuitton, V., R. V. Yelle, and P. Lavvas (2009a), Composition and chemistry of Titan's thermosphere and ionosphere, *Philos. Trans. R. Soc. A*, *367*, 729–741, doi:10.1098/rsta.2008.0233.

Vuitton, V., P. Lavvas, R. V. Yelle, M. Galand, A. Wellbrock, G. R. Lewis, A. J. Coates, and J.-E. Wahlund (2009b), Negative ion chemistry in Titan's upper atmosphere, *Planet. Space Sci.*, *57*, 1558–1572.

Vuitton, V., O. Dutuit, M. A. Smith, and N. Balucani (2014), Chemistry of Titan's atmosphere, in *"Titan: Interior, Surface, Atmosphere, and Space Environment"*, edited by I. C. F. Mueller-Wodarg et al., pp. 224–284, Cambridge Univ. Press, New York.

Wahlund, J.-E., et al. (2009), On the amount of heavy molecular ions in Titan's ionosphere, *Planet. Space Sci.*, *57*, 1857–1865, doi:10.1016/j.pss.2009.07.014.

Waite, J. H., et al. (2004), The Cassini Ion Neutral Mass Spectrometer (INMS) investigation, *Space Sci. Rev.*, *114*, 113–231.

Waite, J. H., D. T. Young, T. E. Cravens, A. J. Coates, F. J. Crary, B. Magee, and J. Westlake (2007), The process of tholin formation in Titan's upper atmosphere, *Science*, *316*, 870–875, doi:10.1126/science.1139727.

Wellbrock, A., A. J. Coates, G. H. Jones, G. R. Lewis, and J. H. Waite (2013), Cassini CAPS-ELS observations of negative ions in Titan's ionosphere: Trends of density with altitude, *Geophys. Res. Lett.*, *40*, 4481–4485, doi:10.1002/grl.50751.

Westlake, J. H., J. H. Waite Jr., K. E. Mandt, N. Carrasco, J. M. Bell, B. A. Magee, and J. -E. Wahlund (2012), Titan's ionospheric composition and structure: Photochemical modeling of Cassini INMS data, *J. Geophys. Res.*, *117*, E01003, doi:10.1029/2011JE003883.

Woods, T. N., F. G. Eparvier, S. M. Bailey, P. C. Chamberlin, J. Lean, G. J. Rottman, S. C. Solomon, W. K. Tobiska, and D. L. Woodraska (2005), Solar EUV Experiment (SEE): Mission overview and first results, *J. Geophys. Res.*, *110*, A01312, doi:10.1029/2004JA010765.

Woods, T. N., et al. (2012), Extreme Ultraviolet Variability Experiment (EVE) on the Solar Dynamics Observatory (SDO): Overview of science objectives, instrument design, data products, and model developments, *Sol. Phys.*, *275*, 115–143, doi:10.1007/s11207-009-9487-6.

Young, D. T., et al. (2004), Cassini plasma spectrometer investigation, *Space Sci. Rev.*, *114*, 1–112, doi:10.1007/s11214-004-1406-4.